

Dynamics and intensity noise suppression in an  
all-polarization-maintaining fiber mode-locked  
laser

*by*

**Sakib Adnan**

A thesis submitted in partial fulfillment of the requirements for the degree of  
Master of Science  
in  
Photonics and Plasmas

Department of Electrical and Computer Engineering  
University of Alberta

© Sakib Adnan, 2021

## Abstract

Recent developments in fiber-based mode-locked lasers have made them increasingly robust and flexible. This development trend makes these lasers more accessible for industrial and scientific applications. In this thesis, we describe the construction and characterization of a robust and flexible all-polarization-maintaining ytterbium-doped fiber laser, mode-locked with a nonlinear amplifying loop mirror. The design of the laser provides robust and easily achievable mode-locking. Moreover, our laser includes “tuning knobs” inside the cavity that provide a great degree of dynamic flexibility in its operation. We utilized this flexibility to implement a novel mechanism for intensity noise suppression and achieve extremely low-noise operation. The pump-to-output transfer bandwidth of the laser was also investigated theoretically and experimentally in order to understand a trade-off between the bandwidth available for active laser stabilization and intensity noise suppression.

# Contents

<b>1</b>	<b>Introduction</b>	<b>1</b>
<b>2</b>	<b>Theoretical background</b>	<b>7</b>
2.1	Nonlinearity, dispersion and soliton formation in mode-locked lasers . . . . .	8
2.2	Derivation of the master equation for passively mode-locked lasers . . . . .	10
2.3	Noise in mode-locked fiber lasers . . . . .	13
2.3.1	Theoretical description of intensity noise . . . . .	14
2.3.2	Theoretical description of timing jitter . . . . .	16
2.4	Theory of pump-to-output transfer function bandwidth in mode-locked fiber lasers . . . . .	18
2.5	Phase-biased NALM-based mode-locked fiber laser . . . . .	21
<b>3</b>	<b>All-PM NALM mode-locked laser construction, analysis and characterization</b>	<b>25</b>
3.1	Laser setup . . . . .	25
3.2	Round-trip transmission analysis . . . . .	29
3.3	Dispersion measurements . . . . .	34
3.4	Mode-locked states characterization . . . . .	37
3.5	Intensity noise characterization and suppression . . . . .	41
3.5.1	Literature review of intensity noise performance and suppression in mode-locked fiber lasers . . . . .	41

3.5.2	Relative intensity noise measurements . . . . .	44
3.5.3	RIN suppression analysis for the mode-locked fiber laser . . . . .	46
3.5.4	Supporting evidence of RIN suppression mechanism theory: output port and rejection port power . . . . .	51
3.5.5	Qualitative estimation of timing jitter trend . . . . .	53
<b>4</b>	<b>Pump-to-output transfer function and anomalous dynamics</b>	<b>55</b>
4.1	Modified master equation . . . . .	56
4.2	Derivation of analytical expressions for loss, self-amplitude modulation and its saturation . . . . .	58
4.3	nonlinear loss and pump-to-output transfer function bandwidth . . . . .	62
4.4	Pump-to-output transfer function bandwidth measurements . . . . .	66
4.5	Transfer bandwidth performance analysis . . . . .	68
4.6	Anomalous dynamics and double pulsing behavior discussion . . . . .	70
<b>5</b>	<b>Conclusion</b>	<b>74</b>
<b>A</b>	<b>Pump noise</b>	<b>85</b>

# List of Figures

1.1	Schematic diagram of a NOLM. The figure is reprinted with permission from [15]. . . . .	3
1.2	Schematic diagram for a NALM laser. The figure is reprinted with permission from [9]. cw: clockwise, ccw: counter clockwise. . . . .	4
2.1	Block diagram model of a passively mode-locked laser. . . . .	11
2.2	Net gain vs. pulse energy. This plot shows unstable behavior with no SAT mechanism (black curve) and stable operation when SAT is present (red curve). The graph is reprinted with permission from [29]. . . . .	19
2.3	(a) Schematic diagram of a “figure-9” NALM-based configuration. (b) Round trip transmission as a function of the nonlinear phase shift difference between waves counter-propagating through the NALM, with no phase-bias (dashed curve) and with a phase bias of $\Delta\varphi_0 = -\pi/2$ (solid curve). The blue part of the solid curve corresponds to the evolution of the laser from noise or continuous-wave operation (at low intensity) to mode-locked operation. The plot and diagrams are reprinted with permission from [9]. FR: Faraday rotator, WP: waveplate, PBS: polarization beam splitter. . . . .	22

3.1	All-PM NALM mode-locked fiber laser consisting of free space and fiber sections. YDF: Yb-doped fiber, WDM: wavelength-division multiplexer, PBS: polarizing beamsplitter, PD: photodiode, HWP: Half-wave plate, QWP: Quarter waveplate. . . . .	27
3.2	Round-trip transmission vs. nonlinear phase shift difference for various orientations of HWP1, with $\theta_q = \theta_o = 0^\circ$ . Calculated with Eq. (3.3). . . . .	32
3.3	Round-trip transmission vs. nonlinear phase shift difference for various orientations of HWP1, with $\theta_q = 45^\circ$ and $\theta_o = 0^\circ$ . Calculated with Eq. (3.3). . . . .	32
3.4	Round-trip transmission vs. nonlinear phase shift difference for various orientations of HWP2, with $\theta_h = \theta_q = 0^\circ$ . Calculated with Eq. (3.3). . . . .	33
3.5	(a) Change in pulse repetition rate vs. central wavelength. (b) GDD values extracted from the measurement (see text for details) (c) Optical spectra recorded for various slit positions. The vertical line indicates the extracted zero dispersion wavelength. . . . .	37
3.6	(a-e) Optical spectra at different pump currents. The dashed line indicates the wavelength at which the intracavity GDD is zero. (f-j) Corresponding RF spectra. In (a-j), the pump current is indicated in the legend. In (a-e), the legend shows the spectral FWHM. . . . .	40
3.7	Examples of low RIN obtained from mode-locked lasers. (a) All-PM phase-biased NALM Yb: fiber laser, reprinted with permission from [8] . (b) NPE Yb: fiber laser, reprinted with permission from [51], (c) SESAM Er:Yb: glass laser, reprinted with permission from [52], (d) Active intensity noise suppression of a SESAM Yb: fiber similariton laser, reprinted with permission from [32]. . . . .	43
3.8	Schematic diagram for RIN measurement. Reprinted with permission from [6]	44

3.9	RIN PSD measured at different pump currents (indicated in the legends in parentheses) for the laser output port and rejection port. The detector background noise level is also shown. . . . .	46
3.10	Calculated round trip transmission, transmission to the output port and transmission to the rejection port, as a function of the nonlinear phase shift difference. The wave plates orientations are $\theta_q = 79^\circ$ , $\theta_h = 40^\circ$ and $\theta_o = 3^\circ$ . . . .	48
3.11	(a) Calculated round trip transmission, transmission to the output port and transmission to the rejection port, as a function of the nonlinear phase shift difference. The wave plates orientations are $\theta_q = 70$ , $\theta_h = 35$ and $\theta_o = 2$ . (b) Output port RIN measured at different pump currents with the same wave plates orientations (taken by Saeid Ebrahimzadeh). . . . .	50
3.12	Output and rejection port power data for different pump current of laser. The plot shows the power measurement where the pump current is varied from (274~512 mA) and all other setting (i.e. waveplate, grating separation) of the oscillator was similar. . . . .	52
3.13	(a) Represents the one of the reading (pump current 372 mA) where the SNR was measured for 11th harmonics of the mode-locked laser,(b)Trend of the SNR with the change in pump current, here it can be visible for higher pump current the SNR is increasing and the laser is moving towards a more stable state. . . . .	53
4.1	Experimental setup for measuring the pump-to-output transfer function of the mode-locked fiber laser. $f_m$ is the frequency of the pump current modulation signal provided by the signal analyzer. PD: photodiode. . . . .	66
4.2	Normalized pump-to-output transfer function at different pump currents. . . .	67
4.3	(a) 3 dB bandwidth of the pump-to-output transfer function vs. pump current, (b) Theoretically calculated normalized bandwidth of the pump-to-output transfer function as a function of nonlinear phase shift difference. . . . .	69

4.4	Experimental measurements for the the anomalous point (pump current of 284 mA) and double-pulsing state (pump current of 512 mA). (a) Optical spectra. (b) RF spectra. (c) Pump-to-output transfer functions. (d) Output port and rejection port power. . . . .	73
A.1	RIN PSD of a laser diode identical to our laser's pump diode, measured at different currents (indicated in the legend). The peak around 50 Hz results from a mechanical vibration in the measurement equipment, and not from the laser. . . . .	85

# List of Tables

3.1	List of components used for the all-PM NALM Yb:fiber laser. . . . .	28
3.2	List of Jones matrices for the components used in the laser. . . . .	30
3.3	Summary of experimentally measured RIN at frequencies that are usually much below, near or much above the relaxation oscillation frequency. The middle column shows the range of values we collected in our literature review. For comparison, the right column shows the RIN values obtained from our laser (see Sections 3.5.2 and 3.5.3 for details). . . . .	44
4.1	Settings used in experimental measurements of the transfer function. . . . .	67

# Acronyms

List of important acronyms

NALM	Nonlinear amplifying loop mirror
PM	Polarization-maintaining
SESAM	Saturable absorber mirrors
NPE	Nonlinear polarization evolution
APM	Additive pulse mode-locking
NOLM	Nonlinear optical loop mirror
cw	Clockwise
ccw	Counter clockwise
MLL	Mode-locked laser
RIN	Relative intensity noise
SAM	Self amplitude modulation
SAT	Saturation of self amplitude modulation
SPM	Self phase modulation
CEO	Carrier-envelope offset
RF	Radio frequency
YDF	Ytterbium doped fiber
CW	Continuous-wave
GVD	Group velocity dispersion
GDD	Group delay dispersion
RTT	Round trip transmission
FR	Faraday rotator
WP	Waveplate
PBS	Polarization beam splitter
ASE	Amplified spontaneous emission
PSD	Power spectral density

WDM	Wavelength division multiplexer
RBW	Resolution bandwidth
VBW	Video bandwidth
SNR	Signal to noise ratio

# Chapter 1

## Introduction

In recent years mode-locked laser sources emitting ultrashort pulses have improved significantly in terms of robustness and flexibility. In particular, mode-locked fiber lasers serve as a compact source for many applications such as terahertz radiation generation [1], precision spectroscopy [2], two-photon microscopy [3], study of attosecond dynamics [4], pure microwave generation [5], and material processing [6, 7]. Because of the high number of implemented and potential applications, the development of robust, flexible, and easy-to-use mode-locked lasers is necessary. Comparing to free space lasers, fiber lasers have several advantages. The most crucial advantage of a fiber laser is its robustness against pump-misalignment. We can deliver pump light from low-cost 976/980 nm semiconductor diode lasers to the gain fiber through all-fiber components. Moreover, gain media such as ytterbium (Yb)- and erbium (Er)-doped glass fibers are very common and easily accessible [8]. Also, fiber lasers have a better thermal management capability because of the higher surface-to-volume ratio.

Fiber-laser mode-locking mechanisms can be divided into two categories: real and artificial saturable absorbers. Examples of real saturable absorbers include semiconductor saturable absorber mirrors (SESAM) [11], graphene [12] and carbon nanotubes(CNT) [13]. Due to design and fabrication complexity, low damage threshold, and their nature of degrad-

ing performance over time, real saturable absorbers have become much less widely used to facilitate mode locking in fiber lasers. Moreover, SESAM mode-locked fiber lasers have slow relaxation. Because of this behavior, this kind of laser has a higher noise floor which dominates all other noise sources such as pump noise [11]. Therefore, here we focus on artificial saturable absorbers.

The robustness and reliability of mode-locked fiber lasers depend on the artificial saturable absorber used for each particular laser. To be specific, lasers that utilize non-polarization-maintaining (PM) fiber are easily impacted by environmental effects such as vibration, thermal fluctuation, etc. The advantages of using non-PM fibers are that this kind of lasers are easy to implement with off-the-shelf optical components with significant flexibility in cavity design. In such lasers, mode-locking can be straightforwardly facilitated via nonlinear polarization evolution (NPE) in standard fiber and an intracavity polarizer [9]. Mode-locking via NPE is only compatible with non-PM fiber because in this technique the polarization needs to have the independence to be freely rotating within the fiber. On the other hand, PM fiber mode-locked lasers are highly robust against environmental influence [9, 10], but require a more involved method of mode-locking.

Nowadays, the most popular group of methods for mode-locking a PM fiber laser using an artificial saturable absorber is additive pulse mode-locking (APM) [14]. These methods were introduced in the early '90s and quickly became very popular due to their fast response and low intrinsic noise. The most widely used APM artificial saturable absorbers, that are compatible with PM fiber, are the nonlinear optical loop mirror (NOLM) [15] and the nonlinear amplifying loop mirror (NALM) [16]. Both of these mechanisms work based on the superposition of two counter-propagating pulses in a fiber loop that can be created by connecting the output ports of an off-the-shelf fiber coupler. The counter-propagating pulses acquire different intensity-dependent phases. When the counter-propagating pulses are combined, they interfere. As always in such interference, intensity is distributed in a manner that depends on relative phase. Since, in this case, the relative phase depends

on initial intensity, the outcome of the interference will depend on the initial intensity of the pulse entering the loop. This means that the intensity of light emitted from the loop is distributed between modes (e.g., with different polarization or direction of propagation) depending on input intensity. In NOLM and NALM, this is used to facilitate artificial saturable absorption by adding an optical element that is more lossy for the mode that corresponds to lower input intensity (e.g., a polarizer or isolator). As noted above, NOLM and NALM-based lasers can be implemented with PM fibers, therefore these lasers can provide very robust and reliable operation.

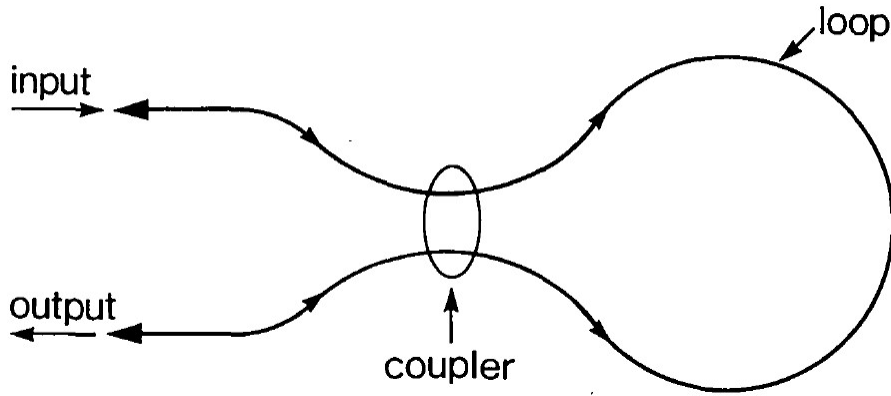


Figure 1.1: Schematic diagram of a NOLM. The figure is reprinted with permission from [15].

Fig. 1.1 shows a schematic diagram of a NOLM laser. To create a mode-locked laser with a NOLM, the loop operates in transmission. The transmission of the loop depends on the nonlinear phase shift difference  $\varphi_{nl}$  between two waves counter-propagating through the fiber loop. This nonlinear phase shift difference is intensity dependent. For a single wave, the non linear phase shift  $\varphi'_{nl}$  is given by [17]

$$\varphi'_{nl} = \frac{2\pi}{\lambda} n_2 I, \quad (1.1)$$

where  $\lambda$  is the wavelength,  $n_2$  is the nonlinear refractive index and  $I$  is the optical intensity. The intensity dependence of the NOLM transmission comes from the asymmetry in the

loop. In the original NOLM configuration, the required asymmetry is generated by an uneven power splitting ratio at the NOLM entrance. This uneven power splitting makes the two counter-propagating waves acquire different nonlinear phase shifts, and therefore their interference depends on intensity, resulting in intensity-dependent NOLM transmission. The main drawback of this particular approach is that, although mode-locking is possible, self-starting mode-lock operation is very difficult to achieve [18]. The reason is that a small deviation of the nonlinear phase shift difference from zero (corresponding to a small variation in intensity) only creates a very small reduction in cavity loss, making it difficult to transition from initial non-pulsed (low-intensity) operation to steady-state pulsed operation.

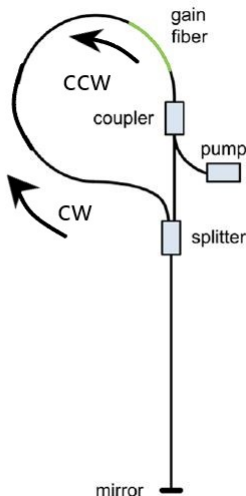


Figure 1.2: Schematic diagram for a NALM laser. The figure is reprinted with permission from [9]. cw: clockwise, ccw: counter clockwise.

Fig. 1.2 shows a schematic diagram of a NALM laser. In a NALM, an amplifying fiber is placed in the loop such that it breaks the symmetry between counter-propagating waves (i.e. clockwise (cw) and counter clockwise (ccw)). This modification improves the situation but still self-starting mode-lock operation is challenging. Recently this issue was addressed through implementation of a non-reciprocal phase bias [16]. The non-reciprocal phase bias facilitates greater variation in loss around  $\varphi_{nl} = 0$ , thereby facilitating self-starting mode-locking. Such phase bias can be generated by using a combination of a Faraday rotator and

wave plates. This technique is explained in detail in section 2.5.

Furthermore, to avoid excessive fiber length, which leads to low pulse repetition rate, the NALM is used in reflection and in combination with a free-space section that contains a mirror at its end. In this reflective design, the power splitting ratio at the NALM input can be fixed or variable according to the configuration of the laser. Due to their robustness, flexibility, and easily achievable self-starting mode-locking behavior, these lasers are becoming more and more popular [9].

The work presented here explores a novel all-PM NALM laser design that was recently developed [8]. This design introduces multiple degrees of freedom that can be dynamically tuned. Our goal is to study how some of these “tuning knobs” could be used to achieve low-noise phase-stabilized operation of our mode-locked laser so that it will generate an optical frequency comb [19, 20]. Towards this goal we characterized the laser’s intensity noise and also its pump-to-output transfer function, since feedback onto the pump power is an established mechanism of frequency comb stabilization. By analyzing the intensity noise and the transfer function’s bandwidth in our laser, we discovered a novel noise-suppression mechanism and studied the trade-off between noise suppression and bandwidth available for stabilization via pump power.

In this thesis, Chapter 2 provides theoretical background on NALM-based mode locking, relative intensity noise and timing jitter. It also includes the master equation for the mode-locked laser, which is used in Chapter 4 to connect laser parameters to the trade-off between noise suppression and stabilization bandwidth. Chapter 3 details the design, characterization and noise performance of our mode-locked laser. In this chapter I explain the impact of each “tuning knob” in our laser. Moreover, the laser is characterized in terms of its optical and radio frequency (RF) spectra, as well as intra-cavity dispersion. In the last part of the chapter, I focus on the noise performance of the laser, including measurements of relative intensity noise (RIN) and qualitative analysis of timing jitter. In Chapter 4, I discuss how different parameters of the master equation such as loss and the saturation of self amplitude

modulation (SAT) can be expressed by using our laser's parameters (i.e waveplate angle and nonlinear phase shift). I also present and analyze experimental measurements of the pump-to-output transfer function of the laser. In the last part of Chapter 4, I present currently-unexplained anomalous experimental results, which are left as subjects for future studies.

# Chapter 2

## Theoretical background

This chapter presents the theoretical background on mode-locking, noise characteristics and pump-to-output transfer function bandwidth of mode-locked fiber lasers. We include the development and important features of the Haus master equation and its perturbation [14]. The theory developed by Haus can be used to analyze various mechanisms of intensity noise, jitter (i.e., pulse timing noise) and phase noise. This thesis mainly focuses on intensity noise, and includes qualitative analysis of jitter.

The robustness of all-PM NALM lasers has motivated their use as frequency combs, which are phase-stabilized mode-locked lasers [19, 20]. Frequency combs have been shown to bring great benefits to many applications, including optical atomic clocks, timing distribution and synchronization, laser ranging and precision spectroscopy [8, 9], to name a few. In the time domain, the output of a stabilized mode-locked laser is a periodic train of pulses, where the time interval between consecutive pulses,  $T_r$ , is fixed. The pulse-to-pulse phase slip of the carrier wave is also fixed. In the frequency domain, this corresponds to a set of narrow spectral features, collectively called a frequency comb. The spacing between each adjacent pair of features (called comb teeth) is the same and equal to the pulse repetition rate,  $f_r = 1/T_r$ . The entire comb structure is offset from the origin by a quantity called the carrier-envelope offset (CEO) frequency,  $f_{CEO}$ , which is related to the pulse-to-pulse phase

slip in the time domain. A stable RF or optical frequency reference can be used to phase-lock the repetition rate and offset frequency and achieve stabilization of the full comb.

A feedback system is required in order to lock a laser to a reference. This system monitors the difference between the laser output and the reference, and correspondingly adjusts some laser parameters to minimize this difference. A very convenient adjustment parameter is the power of the pump laser [28]. Therefore, it is very important to characterize the transfer function between pump power and output. In particular, the bandwidth of this transfer function limits the attainable bandwidth of the stabilizing feedback system.

## 2.1 Nonlinearity, dispersion and soliton formation in mode-locked lasers

This section presents two very important phenomena that play a significant role in describing our laser characteristics. The first one is the nonlinear refractive index and the second is group velocity dispersion (GVD). I will also give a brief overview about how these parameters bring about the formation of solitons.

If the optical intensity is sufficiently high, it can perturb the properties of the medium in which it propagates. This phenomenon results in an intensity dependent contribution to the medium's refractive index [17]:

$$n(I) = n_0 + n_2 I(t). \quad (2.1)$$

Here,  $n_0$  is the unperturbed refractive index,  $n_2$  is the nonlinear refractive index coefficient and  $I$  is the intensity. The phase of light that propagated a distance  $l$  is  $2\pi \cdot n(I) \cdot l/\lambda$ . As a result, the intensity dependence of the refractive index modulates this phase. This effect is called self-phase modulation (SPM) [31]. In a pulse, intensity varies with time, and therefore SPM causes phase to vary with time. Since instantaneous frequency is the time derivative of phase, SPM causes it to vary in time as well.

Group velocity dispersion (GVD) is the dependence of group velocity ( $v_g$ ) on optical frequency ( $\omega$ ) [31] and can be expressed as

$$GVD = \frac{d}{d\omega} \left( \frac{1}{v_g} \right). \quad (2.2)$$

For normal dispersion, the higher frequencies travel slower than the lower ones. The opposite case is called anomalous dispersion. These effects can lead to pulse stretching or compression. Similarly, group delay dispersion (GDD) is the dependence of the group delay on optical frequency, so GDD and GVD essentially describe the same phenomenon. Quantitatively, for a propagation distance  $L$ , the group delay is  $\tau_g = L/v_g$ . Therefore, we have simply  $GDD = d\tau_g/d\omega = L \cdot GVD$ .

Solitons are the result of a balance between SPM and GVD. Both of these processes affect pulse duration by making high frequencies lead or lag behind low frequencies. In the anomalous dispersion regime, GVD and SPM act in opposition to each other. Balancing their actions forms a pulse whose shape remains fixed as it propagates [31]. This kind of pulse is called a soliton. When GVD and SPM are balanced in a mode-locked laser, the laser pulses are solitons [31].

To complete picture of soliton propagation we need to describe the phenomenon of dispersive wave generation [31, 32]. If a soliton is perturbed, by either the generation of additional frequency components or by variation in intensity, the additional light that does not fit into the GVD and SPM balanced soliton will continue to propagate alongside the pulse. This additional light does not form a separate pulse but rather gets very strongly spread temporally due to dispersion and therefore will have very low intensity. For this reason, it is called a dispersive wave.

The above description of soliton formation in mode-locked lasers implicitly assumes that dispersion has a fixed anomalous value throughout the laser cavity. However, there is a class of mode-locked lasers that have large variation in the local value of dispersion in their cavity.

These are called dispersion-managed mode-locked lasers. Their cavity contains elements that impart both normal and anomalous dispersion, such that the net cavity dispersion is close to zero (more precisely, in one cavity round trip, the net GDD has a much smaller magnitude than the positive and negative GDD). Theory, supported by experimental evidence, shows that the pulses that form in such lasers correspond to so-called average solitons [33, 34, 35]. The pulse experiences periodic stretching and compression due to GVD and SPM as it travels through the cavity. Additional filtering effects (e.g., finite gain bandwidth) can also impact pulse duration. Overall, all of these pulse shaping effects need to strike a balance on average in order to sustain a stable pulse train. Therefore, these lasers do have some similarities to soliton lasers, such as dispersive wave generation, in particular when they are operated with net anomalous dispersion.

## 2.2 Derivation of the master equation for passively mode-locked lasers

In a passively mode-locked laser, a nonlinear optical element produces intensity-dependent loss. When mode-locked, the laser produces short pulses, which have much higher peak intensity compared to continuous-wave (CW) or noisy operation. Therefore, mode-locking requires the intracavity loss to decrease with increasing intensity. Passive mode-locking is a dynamic process, in which an ultrashort pulse that is circulating in the laser cavity modulates the intracavity loss, and the intracavity loss modulates the circulating pulse. Through this process, the loss modulation and laser pulse get synchronized and reach a steady state. If the nonlinearity response time is very short, the laser can produce very short pulses.

The nonlinear loss element is called a saturable absorber. A natural saturable absorber is a medium with absorption that decreases as intensity increases. In fiber lasers, artificial saturable absorbers utilize nonlinear phase modulation and interference to create intensity-dependent loss. Intensity depends on both pulse energy and pulse duration, therefore it is

very important to consider nonlinear amplitude modulation, phase modulation and dispersion effects to understand the mode-locking mechanism.

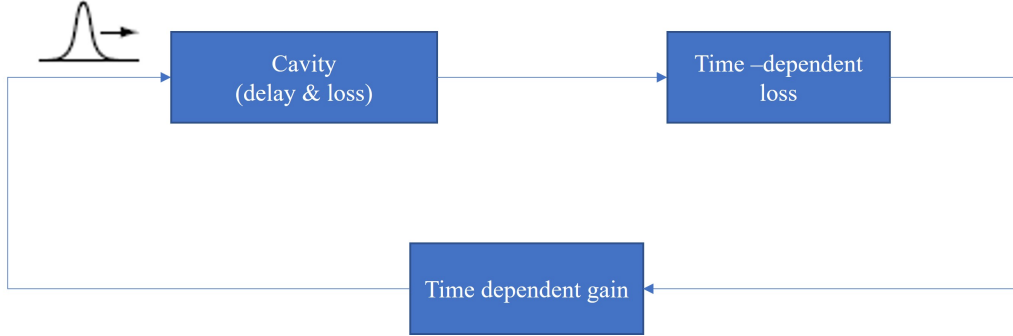


Figure 2.1: Block diagram model of a passively mode-locked laser.

For describing the passive mode-locking process, we consider the changes encountered by a pulse traveling through the cavity during a single round trip [31]. Figure 2.1 shows a block diagram model of a passively mode-locked laser. For simplification of the analysis we assume that the original pulse will be reproduced after a single round trip.

If the initial pulse envelope in the time domain is considered to be  $a(t)$  and the Fourier transform of this envelope is  $A(\omega)$ , the effect of the cavity can be taken into consideration by writing

$$A'(\tilde{\omega}) = e^{-\tilde{\omega}^2/\omega_c^2} e^{-l_0} A(\tilde{\omega}). \quad (2.3)$$

Here,  $\tilde{\omega}$  is defined as  $\tilde{\omega} = \omega - \omega_0$ , where  $\omega_0$  is the center frequency,  $e^{-\tilde{\omega}^2/\omega_c^2}$  is the filtering term related to the finite bandwidth of the optical cavity,  $\omega_c$ , and  $e^{-l_0}$  is the linear time-independent cavity loss. For developing a simplified analytical theory, we assume that the change due to each element per round trip are small, and the mode-locked pulse bandwidth is narrow compared to the filter bandwidth,  $\omega_c$ . If there are no other bandwidth limiting elements, the bandwidth may be determined by the gain bandwidth. Using a Taylor expansion for the above equation we get,

$$A'(\tilde{\omega}) \approx \left(1 - \frac{\tilde{\omega}^2}{\omega_c^2} - l_0\right) A(\tilde{\omega}). \quad (2.4)$$

Applying the inverse Fourier transform gives the corresponding time domain relation,

$$a'(t) \approx \left(1 - l_0 + \frac{1}{\omega_c^2} \frac{d^2}{dt^2}\right) a(t). \quad (2.5)$$

In the same manner we now take into account the nonlinear (and therefore time-dependent) loss  $l(t)$  and gain  $g(t)$ . We assume that the nonlinear loss and gain per pass are small and obtain

$$a''(t) = e^{-l(t)} e^{g(t)} a'(t) \approx \left(1 - l_0 - l(t) + g(t) + \frac{1}{\omega_c^2} \frac{d^2}{dt^2}\right) a(t). \quad (2.6)$$

A mode-locked pulse equation can be derived by taking  $a''(t)$  to be equal to a delayed version of the initial pulse,  $a(t + \delta T)$ . The time shift  $\delta T$  arises from nonlinear pulse shaping by the nonlinear loss  $l(t)$  and gain  $g(t)$ . This shift is usually small compared to the steady state pulse width, and therefore we can approximate the mode-locked state as satisfying

$$a''(t) = a(t + \delta T) \approx a(t) + \frac{da}{dt} \delta T. \quad (2.7)$$

By combining all the above equations we obtain

$$\frac{1}{\omega_c^2} \frac{d^2 a(t)}{dt^2} + [g(t) - l(t) - l_0] a(t) - \delta T \frac{da}{dt} = 0 \quad (2.8)$$

Eq. (2.8) is an example of Haus's Master equation [27]. While deriving the master equation, we considered that per-pass change provided by each element to be a small perturbation. This assumption, which is very realistic for many lasers, allows us to keep only the leading terms in Taylor series expansions. Also, since we're keeping only the constant and linear term, this assumption allows us to arrange the terms in the equation in any order without any effect. The master equation provides analytical insight for a wide range of mode-locking systems.

The master equation can be specialized to the case of APM mode-locking as follows [27].

The nonlinear loss is modeled as a combination of amplitude and phase modulation that result from the SPM-based mode-locking mechanism. This is represented as  $g(t) - l(t) - l_0 = g - l + (\gamma_{SAM} + i\delta)|a|^2$ , where  $g$  is the saturated (time-independent) gain,  $l$  is the linear loss,  $\gamma_{SAM}$  is the self-amplitude modulation (SAM) coefficient and  $\delta$  is the self-phase modulation coefficient (recall that  $|a|^2$  is proportional to intensity). Since nonlinear pulse-shaping effects are now including these terms, we replace  $\delta T$  with  $T_r$ , the pulse repetition period. In fiber APM lasers with no intracavity filter, the finite gain bandwidth acts as an effective filter, which is expressed using the gain dispersion parameter  $D_g$ . Additionally, GVD creates a quadratic dependence of spectral phase on frequency, which Fourier transforms into the operator  $-iD\frac{d^2}{dt^2}$  in the first-order Taylor approximation, where  $D$  is the dispersion parameter. Gain dispersion and GVD are introduced by setting  $\frac{1}{\omega_c^2} = D_g - iD$ . Finally, perturbations are introduced through an additional term,  $V(a)$ . These substitutions, together with separation of time scales, result in the Haus's master equation for a mode-locked fiber laser,

$$T_r \frac{da}{dT} = (g - l)a(T) + (D_g - iD)\frac{d^2 a}{dt^2} + (\gamma_{SAM} + i\delta)|a|^2 a(T) + V(a). \quad (2.9)$$

Here the envelope  $a(t, T)$  is a function of the time  $t$  on the timescale of a pulse and the much slower time  $T$  on the timescale of a round-trip time. In section 4.1, we discuss a modification of the master equation parameters to match our laser parameters, which we use to derive an expression for the pump-to-output transfer function bandwidth for our laser.

## 2.3 Noise in mode-locked fiber lasers

Noise is an important factor for the commercialization of mode-locked fiber lasers. When mode-locked lasers are used in high precision applications, low-intensity noise is an important requirement. Some relevant examples where intensity noise management for mode-locked lasers are important are optical communication systems, spectroscopy, photonic digital to analog converters, optical sampling, precision magnetometry and being used as a seed for

optical amplifiers. Moreover, the intensity noise of mode locked lasers can impact laser performance indirectly by coupling intensity noise to  $f_{CEO}$  noise (comb lines fluctuation) conversion in frequency combs or even by amplitude to phase conversion of photo-detectors in microwave generation [29].

The electric field of an optical pulse train is given by [43]

$$A(t) = [A_0 + \Delta A_0(t)] \sum_{n=-\infty}^{\infty} a(t - nT_r + \Delta T_r(t)) \exp[j \{2\pi\nu_c t + n\Phi_{CE} + \Delta\theta(t)\}]. \quad (2.10)$$

Here,  $A_0$  is the amplitude and  $\Delta A_0(t)$  is amplitude noise. The pulse envelope function is  $a(t)$ , the pulse repetition period is  $T_r$ ,  $\Delta T_r(t)$  is the pulse timing jitter,  $\nu_c$  is the carrier frequency,  $\Phi_{CE}$  is the pulse-to-pulse carrier-envelope phase slip, and  $\Delta\theta(t)$  is the phase fluctuation of the field. The latter was included here for completeness so that the equation represents all the noise feature of a mode-lock fiber laser. For the remainder of this thesis, we ignore carrier phase noise, as it is beyond the scope of this work.

As mentioned above, in this work we are concerned with two noise factors of mode-lock fiber lasers: the amplitude noise,  $\Delta A_0(t)$ , which will be recast as the intensity noise, and the timing jitter  $\Delta T_r(t)$ , which will be treated as the repetition-rate phase noise in the frequency domain.

### 2.3.1 Theoretical description of intensity noise

Intensity noise can be defined as the fluctuation of the optical pulse train's average power over a specific measurement time span, that defines the average power stability of that particular optical pulse train. We write the optical power of the pulse train as

$$P(t) = P_{avg} + \Delta P(t). \quad (2.11)$$

Here,  $P_{avg}$  is the average power of the pulse train and  $\Delta P(t)$  is the optical power fluctuation. The intensity noise is quantified using relative intensity noise (RIN) [46], given by

$$RIN = \frac{\langle \Delta P(t)^2 \rangle_T}{\langle P(t) \rangle_T^2}, \quad (2.12)$$

where  $\langle P(t) \rangle_T^2$  is the square of the pulse train average optical power, and  $\langle \Delta P(t)^2 \rangle_T$  is the mean squared optical power, for a specific measurement time  $T$ . Equivalently, RIN can be described using its power spectral density (PSD) in the frequency domain:

$$S_{RIN}(f) = \frac{1}{P_{avg}^2} \int_{-\infty}^{\infty} \langle \Delta P(t) \Delta P(t + \tau) \rangle e^{-j2\pi f \tau} d\tau. \quad (2.13)$$

Here, the PSD depends on the noise at frequency  $f$ . This expression, as given by Wiener [31], was obtained by taking the Fourier transform of the optical power's autocorrelation function. Conveniently, the PSD can be measured with an RF spectrum analyzer and a photodiode. The unit of RIN PSD is  $Hz^{-1}$ , and it is commonly specified on a logarithmic scale as dBc/Hz. Furthermore, the PSD can be integrated over a specific frequency range to yield the mean square value of relative intensity noise over that range of frequencies.

Quantum and semi-classical intensity noise theory and experimental analysis for single-frequency lasers was carried out by Harb. et. al. [44, 45]. This experimental and theoretical analysis for single-frequency lasers can be used to explain the intensity noise of femtosecond mode-locked laser [6], since we are dealing with time-averaged power. Intensity noise in mode-lock fiber lasers is mainly caused by two factors. The first is external technical noise sources and the second one is quantum noise sources. The pump laser's intensity noise is an example of an external noise source. Amplified spontaneous emission (ASE) is an example of a quantum source of intensity noise.

As described in Section 2.4, a small perturbation of the laser's gain will trigger a transient oscillation relaxation that will fade away exponentially. Overshoot may be observed at the relaxation oscillation frequency in the frequency domain. The output response behaves like

a low pass filter output and it rolls off quickly after the relaxation oscillation frequency. In the case of Yb-doped mode-locked fiber lasers, the gain medium relaxation time is in the ms range, or equivalently in the frequency domain, it is on the order of a kilohertz. Both ASE and pump noise usually contribute the output RIN at frequencies below and up to the relaxation oscillation frequency. Usually, the pump noise level is much higher than the ASE noise level. As a result, the RIN of mode-locked fiber lasers is usually dominated by the pump noise for frequencies lower than the relaxation oscillation frequency.

Far above the relaxation oscillation frequency, RIN approaches the quantum noise limit. Then the noise floor is set by the shot noise [6] that enters the cavity through the output coupler. The corresponding PSD is given by

$$S_{RIN}^{shot-noise}(f) = \frac{2h\nu_c}{P_{avg}}, \quad (2.14)$$

where  $h$  is the Planck constant. This description of RIN is used in Section 3.5.2

### 2.3.2 Theoretical description of timing jitter

Timing jitter is the deviation of an optical pulse train from perfect periodicity. Timing jitter is a bit different than the intensity noise because intensity fluctuation can be defined as a stationary process, so we could use the Fourier transform of an autocorrelation function to derive a PSD. Also, as explained in Section 2.4, gain saturation works towards quenching intensity noise in a free-running mode-locked fiber laser. There is no such restoring force that acts to suppress timing jitter.

Consider a simplified case, where dispersion is zero (so the pulse shape doesn't change) and the observation time is much longer than the pulse repetition period. Then the timing jitter will be proportional to the observation time [43] and can be treated as a stationary

process. The corresponding timing jitter power spectral density can be written as

$$S_{\Delta T}(f) = \int_{-\infty}^{\infty} \langle \Delta T_R(t) \Delta T_R(t + \tau) \rangle e^{-j2\pi f\tau} d\tau. \quad (2.15)$$

This expression shows that greater timing jitter, meaning a narrower autocorrelation function, will appear as a broadening of the PSD.

When the pulse train is detected by a photodiode, it beats against itself, effectively producing the pulse train's autocorrelation function. Due to the pulse train's periodicity, this beating produces a series of spectral features at harmonics of the repetition rate. Since these are RF frequencies, these spectral features can be measured easily. The shape of each of these features is determined by the PSD of the various noise contributions. Let us assume for a moment that intensity noise and jitter are entirely independent of each other. In the time domain, all pulses in the train share the same effective amplitude modulation due to intensity noise. Correspondingly, in the frequency domain, all harmonics of the repetition rate get the same contribution from intensity noise. This is not the case for jitter; each pulse gets shifted by a different random time interval. Over a long period of time, corresponding to low frequencies, the jitter autocorrelation gets reduced. As frequency increases, so does the impact of jitter on the observed spectrum. Therefore, the timing jitter PSD can be obtained by measuring the spectrum of one of the higher harmonics in repetition rate using high-speed photodetection. If the intensity noise and timing jitter are correlated (as may result from self-phase modulation), such measurements can be used to obtain an upper bound on the jitter's contribution to noise.

## 2.4 Theory of pump-to-output transfer function bandwidth in mode-locked fiber lasers

In general, in any kind of feedback system, a higher feedback bandwidth is preferred. However, it was experimentally observed that, when feeding back on the pump power, the feedback bandwidth is limited to the KHz range [28]. An important question is which parameter limits the feedback bandwidth. While usually the laser dynamics (timescale of a round-trip, about 10 ns) is much faster than the dynamics of the popularly used gain media (e.g. Yb: fiber, where relaxation time is about 1 ms), they are still coupled to each other. Because of this interplay, the time-dependent response of laser dynamics due to a change in pump power is complicated.

SAM, gain, and loss determine the pulse energy-dependent gain for mode-locking. However, as previously mentioned, the gain medium usually has a slow response compared to the fast laser dynamics. Therefore, gain saturation alone cannot stabilize the laser. To stabilize the system against perturbations a fourth component needs to be included in the cavity [29], which is called saturation of the self-amplitude modulation (SAT). This saturation is a form of energy-dependent loss. It can be manifested physically by the generation of Kelly sidebands (sidebands in the optical spectrum of some mode-locked lasers, which are created by a periodic disturbance of soliton pulses that lead to excessive dispersive wave generation) or rollover of the SAM (i.e., above some value of pulse energy, loss increases with energy) [30]. The SAT parameter provides stability to the laser by causing the net gain to decrease with an increase in the pulse energy, which can result from a change in pump power or perturbations. This behavior corresponds to a negative slope of the net gain when plotted against pulse energy, above some level of energy (see Figure.2.2 ). The negative slope can be characterized by a nonlinear loss parameter  $\eta$ . The value of  $\eta$  depends on the technical details of the laser system. A higher the value of  $\eta$  represents higher stability for that particular laser system, since a higher value of  $\eta$  means stronger damping of fluctuations. By

using the theory given by Newbury et. al. [29, 30]  $\eta$  can be expressed as

$$\eta = \alpha_3(g - l) + \alpha_4\gamma_{sat}w^4, \quad (2.16)$$

where  $\alpha_3$  and  $\alpha_4$  are constants and  $w$  is pulse energy.

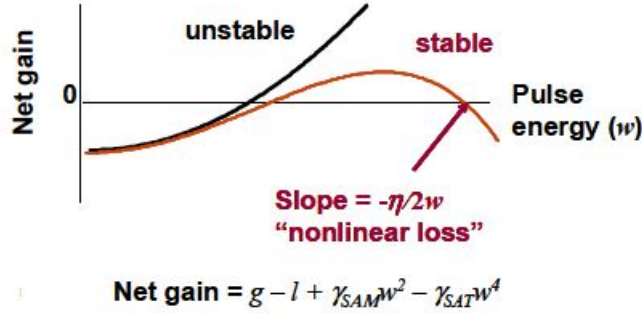


Figure 2.2: Net gain vs. pulse energy. This plot shows unstable behavior with no SAT mechanism (black curve) and stable operation when SAT is present (red curve). The graph is reprinted with permission from [29].

Over a time scale much longer than the cavity round-trip, an increase in pulse energy ( $w$ ) reduces the gain ( $g$ ) due to gain saturation caused by the circulating optical power. We denote the gain medium's relaxation time as  $T_g$  and the cavity round trip time  $T_r$ . Then the coupled evolution, over a long time scale  $T$ , of perturbations in the gain,  $\Delta g$ , and pulse energy,  $\Delta w$ , due to a perturbation in the pump power,  $\Delta P$ , is described by [30]

$$\partial_T \Delta w = -\frac{1}{T_r} [\eta \Delta w - 2\Delta g \Delta w] \quad (2.17)$$

$$\partial_T \Delta g = -\frac{1}{T_g} \left[ \Delta g + g_w \frac{\Delta w}{w} - g_P \frac{\Delta P}{P} \right], \quad (2.18)$$

here the pump power,  $P$ , is measured relative to threshold. The first equation is a direct mathematical description of Figure 2.2. The second equation describes the exponential decay of the gain to the steady state value. Here,  $g_w = -wdg/dw$  and  $g_P = Pd g/dP$ . Using a

saturable Lorentzian to model the gain transition, Newbury et al. [30] have shown that when the pump power greatly exceeds the gain medium's saturation power, which is the regime considered here, we have  $g_p = g_w = 1/2$ .

The solution of these equations is a decaying exponential, corresponding to the laser gradually approaching a new steady-state operation following a small change in pump power. From this solution we obtain the relation between the 3 dB bandwidth of the laser's response,  $\nu_{3dB}$ , and the nonlinear loss,  $\nu_{3dB} = (1 + \eta^{-1})\nu_{3dB}^g$ , where  $\nu_{3dB}^g = \frac{1}{2\pi T_g}$ . Here  $\nu_{3dB}^g$  is the response bandwidth of the gain medium only. From Eq. (2.17), the steady-state solution for changes in gain and pulse energy caused by a change in pump power is

$$dw/dP = 2w\eta^{-1}(dg/dP) \quad (2.19)$$

$$dg/dP = \frac{\nu_{3dB}^g}{\nu_{3dB}}(2P)^{-1}. \quad (2.20)$$

ere we took  $g_p = g_w = 1/2$  and  $\Delta w/\Delta P = dw/dP$ .

This theory provides important insights into mode-locked fiber laser dynamics. First, the bandwidth of the laser's response to perturbation will exceed the bandwidth of the gain medium's response,  $\nu_{3dB} > \nu_{3dB}^g$ . This is a result of the laser dynamics being much faster than the gain dynamics, as explained above. Second, a higher value of the nonlinear loss  $\eta$  (corresponding to the laser response bandwidth becoming smaller and closer to gain response bandwidth) leads to higher stability (i.e., stronger attenuation of perturbations outside the laser response bandwidth). This understanding will play a role in section 4.5 to explain the pump-to-output transfer function bandwidth of our laser.

A final note is due in order to place this analysis in the context of our work. Our goal is to stabilize the laser frequency by modulating the pump power. The analysis presented here concerns the response of the output power - and not frequency - to variation in pump current. However, they are directly related. The reason is that if we modulate the pump power, it will modulate the laser intensity. From section 2.1, we see that modulating the in-

tensity modulates the nonlinear refractive index which in turn modulates the laser frequency. In summary, when we modulate the pump power and measure the output power response dynamics, we are effectively measuring the response dynamics of the laser frequency. Measuring the output power response is practically easier than measuring the response of the laser frequency. In such experiments [29], including the one presented here, it is common to measure the output power response for determining the pump to frequency transfer function bandwidth.

## 2.5 Phase-biased NALM-based mode-locked fiber laser

In a NALM-based mode-locked laser the NALM can be used in various ways to facilitate mode-locking [16]. In the configuration that is used in this thesis the NALM is made entirely of PM fiber and it is used in reflection as shown schematically in Fig. 2.3 (a). With this particular configuration, it is possible to have a fast-increasing round trip transmission with increasing intensity (i.e., effective saturable absorption), for very low intensity [9]. This means that self-starting mode-locking is easy to achieve.

The nonlinear phase shift difference between the two waves counter-propagating through the loop,  $\Delta\varphi_{nl}$ , is proportional to intensity, with a proportionality factor that depends on technical details of the laser (e.g., fiber length). Below we use the phase shift difference instead of intensity as a more universal parameter for describing laser dynamics.

Before explaining the concept of the non-reciprocal phase bias and how it is achieved, we discuss its effect on the laser to explain its significance. Figure 2.3(b) shows the round trip transmission function without any non-reciprocal phase bias (dashed curve) and with a non-reciprocal phase bias of  $-\pi/2$  (solid curve). With no phase bias, the round-trip transmission peaks at  $\varphi_{nl} = 0$  and drops away for higher nonlinear phase shifts, therefore mode-locking cannot be started. The phase-bias shifts the entire curve such that it has a positive slope around  $\Delta\varphi_{nl} = 0$ , which facilitates self-starting mode locking.

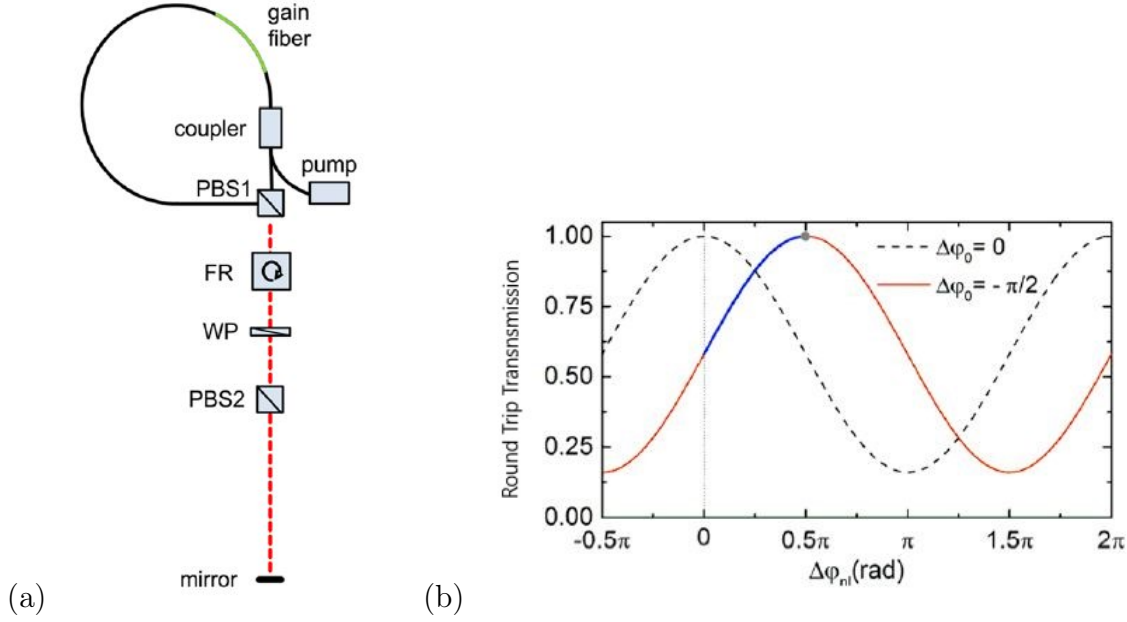


Figure 2.3: (a) Schematic diagram of a “figure-9” NALM-based configuration. (b) Round trip transmission as a function of the nonlinear phase shift difference between waves counter-propagating through the NALM, with no phase-bias (dashed curve) and with a phase bias of  $\Delta\varphi_0 = -\pi/2$  (solid curve). The blue part of the solid curve corresponds to the evolution of the laser from noise or continuous-wave operation (at low intensity) to mode-locked operation. The plot and diagrams are reprinted with permission from [9]. FR: Faraday rotator, WP: waveplate, PBS: polarization beam splitter.

Fig. 2.3 (a) shows a schematic NALM-based mode-locked laser diagram. In this configuration, a waveplate and a  $45^\circ$  Faraday rotator are placed between two polarization beam splitters. The PM fiber that connects the ports of PBS1 on the NALM side is twisted by  $90^\circ$  so that the polarization component transmitted at the entrance of the NALM will be reflected at its exit, and vice versa. The gain fiber is placed asymmetrically in the loop, i.e. not at the center of the loop. Below we explain how this configuration achieves self-starting mode-locking by examining the dependence of the round-trip transmission ( $T_{RTT}$ ) on intensity. This transmission can be obtained quantitatively, to produce Fig. 2.3 (b), by analyzing the polarization evolution of the intracavity electric field using Jones calculus [41].

As a first step, consider the case where the WP in Fig. 2.3 (a) is absent and the gain medium provides a gain of 1. Then, going upwards from PBS2, we have horizontal polarization. After the FR we get polarization at 45 degrees clockwise from horizontal. In the loop,

half of the power goes to the clockwise (cw) direction and half will go to counterclockwise (ccw) propagation direction. Since the gain is set to 1, both counter-propagating components have the same intensity throughout the loop, and therefore they obtain identical nonlinear phase shifts, i.e.  $\Delta\varphi_{nl} = 0$ . After the loop, the vertical and horizontal polarization components swap places (because the fiber is twisted), resulting in polarization at 45 degrees counter-clockwise from horizontal. The FR then rotates the polarization to horizontal and the light is fully transmitted through PBS2. Therefore, the round-trip transmission is at its maximum,  $T_{RTT} = 1$ . This situation corresponds to  $\Delta\varphi_{nl} = 0$  on the dashed curve in Fig. 2.3 (b).

As a second step, consider the case where the WP in Fig. 2.3 (a) is absent and the gain medium provides a gain greater than 1. Since the gain fiber is placed off-center in the loop, the ccw component will get amplified before propagating in the long passive fiber, while the cw component will only get amplified after passing through the long section of the loop. Therefore, the ccw component will pick up a greater nonlinear phase shift than the cw component, i.e.  $\Delta\varphi_{nl} > 0$ . Since the round-trip transmission is at its maximum for  $\Delta\varphi_{nl} = 0$ , it can only decrease as  $\Delta\varphi_{nl}$  increases from 0, as shown by the dashed curve in Fig.2.3(b). We can understand this physical mechanism by considering the NALM to be an intensity-dependent waveplate: the nonlinear phase-shift difference between the counter-propagating orthogonally-polarized components determines the polarization at the loop's output. After the FR and waveplate, both of the loop's polarization components have contributions along the axes of PBS2, where they interfere. The resulting transmission depends on their relative phase, which in turn depends on their relative nonlinear phase shift. Achieving mode-locking is very difficult (to the point of impracticality) in this situation. The reason being, before mode-locking, the laser goes into CW (continuous-wave) or noisy operation, which has much lower intensity than pulsed operation. This lower intensity results in almost zero nonlinear phase shift in the NALM, even if the pump power is very high. Therefore, the laser is initially around  $\Delta\varphi_{nl} = 0$  where  $T_{RTT} = 1$ , and any perturbation that increases intensity is

immediately quenched by the increased loss (i.e., reduction in  $T_{RTT}$ ).

As a final step, consider the case where the WP in Fig. 2.3 (a) is present and it is a  $\lambda/8$  plate oriented at 45 degrees. Then, in one round-trip, the waveplate adds a  $\pi/2$  phase shift between its slow and fast axes, which we call the phase bias. These fixed phase bias and intensity-dependent phase difference provided by the NALM result in the solid curve in Fig.2.3(b), which is shifted from the dashed curve by  $\pi/2$ . In this case, at low intensity (near  $\Delta\varphi_{nl} = 0$ ), the round-trip transmission strongly increases with increasing intensity (i.e., increasing  $\Delta\varphi_{nl}$ ). As a result, the laser will favor pulsed operation and mode-locking can be achieved easily. It is important to note that the biasing action of the waveplate is made possible by the non-reciprocity of the FR, and that is why its effect is called a non-reciprocal phase-bias.

Our laser system uses the same configuration as described above, except that we have additional components (wave plates and diffraction gratings) that provide additional degrees of freedom. These additional components which allow us to tune the laser parameters and manipulate its operation. This is detailed in section 3.1.

# Chapter 3

## All-PM NALM mode-locked laser construction, analysis and characterization

This chapter details the design, operation and characterization of an all-PM NALM mode-locked Yb: fiber laser, including experimentally measured intensity noise and jitter. We demonstrate a novel mechanism of intensity noise suppression and achieve operation with very low RIN of  $-156$  dBc/Hz at frequencies above 100 Hz.

### 3.1 Laser setup

The mode-locked all-PM NALM Yb: fiber laser that we constructed and used for our experiments is schematically depicted in Fig. 3.1. This design was first introduced in [36]. The laser is constructed with the collaboration of the same group in Vienna. Essentially this laser is a practical and modified implementation of the concept described in section 2.5. Here the  $\lambda/8$  waveplate from the schema of Fig. 2.3 is replaced with a combination of quarter waveplate (QWP) oriented at an angle  $\theta_q$  and a half waveplate (HWP1) oriented at an angle  $\theta_h$ . PBS1 from Fig. 2.3 is replaced by a polarization beam combiner and collimator (PBCC).

The PBCC provides polarization beam splitting/combining and also works as a free space to fiber coupler. To control the output coupling rate an additional half waveplate (HWP2) oriented at an angle  $\theta_o$  is introduced to the left of the PBS. Lastly, a grating pair is also included in the cavity to control the overall cavity dispersion, i.e., this is a dispersion-managed laser. Each grating diffraction efficiency is about 94%. By controlling the separation between the gratings we can control the net dispersion of the laser. Our main goal was to keep the net dispersion close to zero and slightly negative to achieve low noise operation [37, 38]. The dispersion measurement of our laser is given in section 3.3. Finally, a silver mirror is placed after the grating pair to complete the free space section. The free space section length is about 30 cm.

We placed an isolator between the pump diode and the fiber loop to prevent any light from reaching the pump diode. A wavelength division multiplexer (WDM) is used so that it passes the pump light at 976 nm and reflects light with wavelength in the range 1020-1100 nm. One arm of the WDM is spliced to one of two ports of the PBCC and the other arm is spliced to a 49 cm long Yb-doped PM fiber, with about 32 cm of passive fiber between the active fiber and WDM splicing. The loop is then completed by splicing the active fiber with the other port of the PBCC, where 47 cm of passive fiber remains between the active fiber and the PBCC.

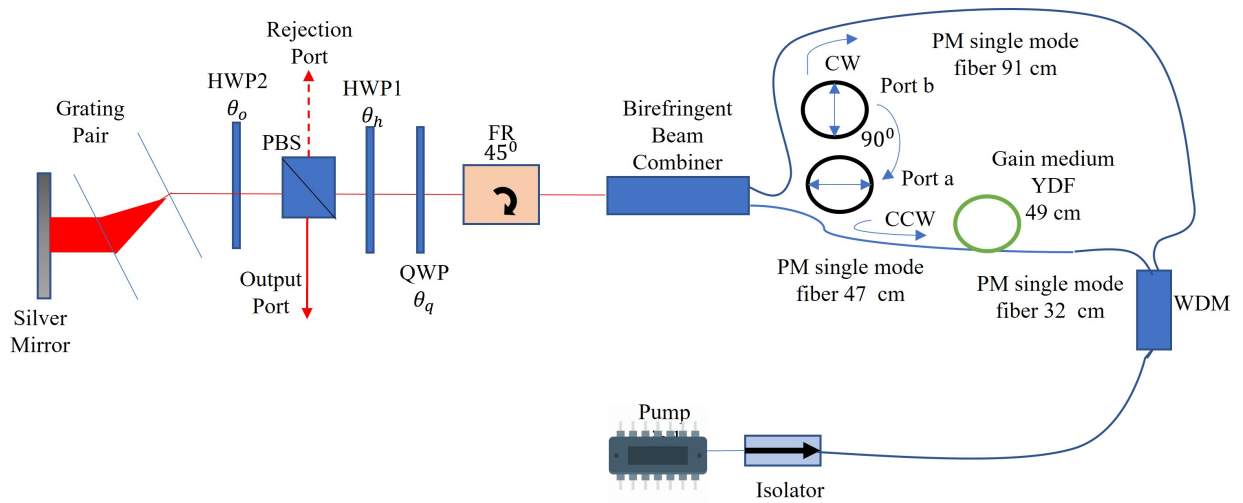


Figure 3.1: All-PM NALM mode-locked fiber laser consisting of free space and fiber sections. YDF: Yb-doped fiber, WDM: wavelength-division multiplexer, PBS: polarizing beamsplitter, PD: photodiode, HWP: Half-wave plate, QWP: Quarter waveplate.

Table 3.1 details the components used to construct this laser. The WDM has an insertion loss of 1 dB for the pump. A passive single-mode PM fiber (SM98-PS-USD-H) is used as the pigtailed fiber for the common port of the WDM. If the cavity has a design of near-zero net anomalous dispersion then it facilitates low-noise soliton mode-locking [47]. Therefore, we tried to keep the group delay dispersion of the laser to be close to zero. To increase the cw/ccw asymmetry in the fiber loop for facilitating self-starting mode-locking, we used different lengths of passive PM fibers on either side of the gain fiber.

Component Name	Description
Laser diode	Thorlabs BL976-PAG900 is a 976 nm, 900 mW FBG-stabilized laser with a PM fiber output and FC/APC connector.
Gain fiber	Coractive Yb 401-PM, 49 cm length, $0.02\text{ps}^2/\text{m}$ , 250 dB/m absorption at 975 nm, Panada type Yb-doped PM optical fiber.
Single mode PM fiber	Thorlabs PM-980 nm PM fiber.
Pump isolator	AFR HPMI-SS-01-N-B-Q-F-1-C, Rev11C, wavelength range $976\pm 10$ nm, 1 W maximum average optical power, fast axis blocked, Corning PM 980 fiber.
Wavelength division multiplexer	AFR PMFWDM-9806-N-B-Q-P, SR8432, PM WDM, pass band 960-990 nm, reflection band 1020-1080nm, maximum avg power 3W, maximum peak power 1 kW.
Polarization beam combiner and collimator	AFR Semi-PBCC-03-09-N-B-Q, SR17551, birefringent polarizing beam combiner with collimated beam output, operation wavelength 1030 nm, beam diameter 0.9 mm, PM 980 Panda fiber.
Faraday rotator	EOT HP-05-R-1030, rotation @ 1030 nm: $45^\circ \pm 0.5^\circ$ .
Gratings	LightSmyth T-1000-1040-3212-94, 1000 lines/mm, angle of incidence (Littrow) $31.3^\circ$ , diffraction efficiency for s and p polarizations $>94\%$ .
End mirror	Thorlabs PF03-03-P01, protected silver mirror with 7.0 mm diameter.

Table 3.1: List of components used for the all-PM NALM Yb: fiber laser.

The total length of fiber in our laser is about 218 cm. The refractive index of the fiber is  $n \approx 1.5$ . The resulting repetition rate of the laser is  $f_{rep} = \frac{c}{2L+nL_f} \approx 77.519\text{MHz}$ . Here  $L$  is the free space cavity length,  $L_f$  is the fiber length and  $c$  is the speed of light in vacuum. This result is very close to the experimentally measured repetition rate of 75.515 MHz, verifying the lengths and distances we measured.

## 3.2 Round-trip transmission analysis

In this section we use Jones calculus to derive a general expression for the laser cavity round-trip transmission and demonstrate the impact of the various waveplates orientation on this transmission. Table. 3.2 contains the Jones matrices for the optical elements in the cavity. All angles are measured with respect to the horizontal in the lab frame, and they indicate the orientation of the fast axis of a birefringent optic. The nonlinear phase shift is introduced as an independent parameter via its own Jones matrix. The polarization variation due to a single pass through the grating pair has been experimentally found to be equivalent to a QWP with its fast axis along the horizontal [8].

Component Name	Jones Matrix
Faraday rotator	$M_{FR}(\theta_{FR}) = \begin{bmatrix} \cos\theta_{FR} & \sin\theta_{FR} \\ -\sin\theta_{FR} & \cos\theta_{FR} \end{bmatrix}$
Half waveplate	$M_{\lambda/2}(\theta_h) = e^{(-i\pi/2)} \begin{bmatrix} \cos^2\theta_h - \sin^2\theta_h & 2\cos\theta_h\sin\theta_h \\ 2\cos\theta_h\sin\theta_h & \sin^2\theta_h - \cos^2\theta_h \end{bmatrix}$
Quarter waveplate	$M_{\lambda/4}(\theta_q) = e^{(-i\pi/4)} \begin{bmatrix} \cos^2\theta_q + i\sin^2\theta_q & (1-i)\cos\theta_q\sin\theta_q \\ (1-i)\cos\theta_q\sin\theta_q & \sin^2\theta_q + i\cos^2\theta_q \end{bmatrix}$
Grating pair	$M_{gratings} = e^{(-i\pi/4)} \begin{bmatrix} 1 & 0 \\ 0 & i \end{bmatrix}$
Output coupling HWP	$M_{\lambda/2}(\theta_o) = e^{(-i\pi/2)} \begin{bmatrix} \cos^2\theta_o - \sin^2\theta_o & 2\cos\theta_o\sin\theta_o \\ 2\cos\theta_o\sin\theta_o & \sin^2\theta_o - \cos^2\theta_o \end{bmatrix}$
End mirror	$M_{Silver} = \begin{bmatrix} -1 & 0 \\ 0 & -1 \end{bmatrix}$
PBS	$M_{PBS,transmission} = \begin{bmatrix} 1 & 0 \\ 0 & 0 \end{bmatrix}, M_{PBS,reflection} = \begin{bmatrix} 0 & 0 \\ 0 & 1 \end{bmatrix}$
Twisted PM fiber loop	$M_{loop} = \begin{bmatrix} 0 & 1 \\ 1 & 0 \end{bmatrix}$
Nonlinear phase shift	$M_{nl(\Delta\Phi_{nl})} = \begin{bmatrix} e^{(i\Delta\Phi_{nl})} & 0 \\ 0 & 1 \end{bmatrix}$

Table 3.2: List of Jones matrices for the components used in the laser.

In our laser, the geometric asymmetry around the gain fiber in the loop increases the nonlinear phase shift difference  $\Delta\varphi_{nl}$  as compared to a symmetric geometry with the same input power splitting ratio. The second contributing factor to  $\Delta\varphi_{nl}$  is the (adjustable) asymmetric splitting ratio at the input to the NALM. The nonlinear phase shift difference can be expressed as the nonlinear phase difference between port a and port b (see Fig. 3.1), where  $\Delta\varphi_{nl} = \varphi_{nl}^a - \varphi_{nl}^b$ ,  $\varphi_{nl}^a$  is the nonlinear phase of the ccw wave that travels in ccw from port a to port b, and  $\varphi_{nl}^b$  is the nonlinear phase obtained by the cw wave 2 that travels from port b to port a. The gain medium is much closer to port a than to port b. Therefore, over almost the entire range of splitting ratios, the nonlinear phase accumulated by the ccw wave will be greater than the nonlinear phase accumulated by the cw wave, i.e.  $\Delta\varphi_{nl} > 0$ .

We will now derive an analytical expression for the cavity's round-trip transmission. The

field immediately to the right of the PBS is horizontally polarized,

$$E_{in} = \begin{bmatrix} 1 \\ 0 \end{bmatrix}, \quad (3.1)$$

where we normalized this field's intensity to 1. The intracavity electric field after one round-trip is given by  $E_{intra}^{rt}(\theta_q, \theta_h, \theta_o, \Delta\Phi_{nl}) =$

$$\begin{aligned} & M_{PBS2TX} M_{\lambda/2}(\theta_o) M_{gratings} M_{Silver} M_{gratings}(0^\circ) \times \\ & M_{\lambda/2}(\theta_o) M_{PBS2TX} M_{\lambda/2}(\theta_h) M_{\lambda/4}(\theta_q) M_{FR}(45^\circ) \times \\ & M_{loop} M_{nl}(\Delta\Phi_{nl}) M_{FR}(45^\circ) M_{\lambda/4}(\theta_q) M_{\lambda/2}(\theta_h) E_{in}. \end{aligned} \quad (3.2)$$

Since the intensity has been normalized to 1, the round-trip transmission is given by the squared modulus of the field after one round-trip:  $T_{RTT} = |E_{intra}^{rt}(\theta_q, \theta_h, \theta_o, \Delta\Phi_{nl})|^2 =$

$$\begin{aligned} & \frac{1}{4} \cos^2(4\theta_o) \left[ \cos^2\left(\frac{\Delta\Phi_{nl}}{2}\right) \left\{ 4\sin^2(2\theta_q) + \left\{ \sin(4\theta_h) - \sin(4\theta_q - 4\theta_h) \right\}^2 \right\} + \right. \\ & \left. 4\sin^2\left(\frac{\Delta\Phi_{nl}}{2}\right) \cos^2(4\theta_h - 2\theta_q) + 2\sin(\Delta\Phi_{nl}) \cos(4\theta_h - 2\theta_q) \left\{ \sin(4\theta_h) - \sin(4\theta_q - 4\theta_h) \right\} \right]. \end{aligned} \quad (3.3)$$

The round-trip transmission depends on four parameters: the orientation angles of HWP1, QWP, HWP2 and the nonlinear phase shift (controlled via the pump current). These serve us as tuning knobs for controlling the laser operation. The Jones vectors of light at the rejection port,  $E_{rej}^{rt}$ , and output port,  $E_{Out}^{rt}$ , can be calculated in a similar manner.

We can use Eq. (3.3) to demonstrate the effect of waveplate orientation on the round-trip transmission. For example, Fig. 3.2 shows the round-trip transmission vs. nonlinear phase shift difference for various values of  $\theta_h$ , while  $\theta_q$  and  $\theta_o$  are kept fixed at  $0^\circ$ . In this case, rotating HWP1 directly varies the phase bias without affecting the modulation depth. Fig. 3.3 shows a similar plot, where this time  $\theta_q = 45^\circ$ . In this case, rotating HWP1 varies the

modulation depth without any impact on the phase bias. In the general case, where  $\theta_q$  has an arbitrary value, rotating HWP1 will affect both phase bias and modulation depth.

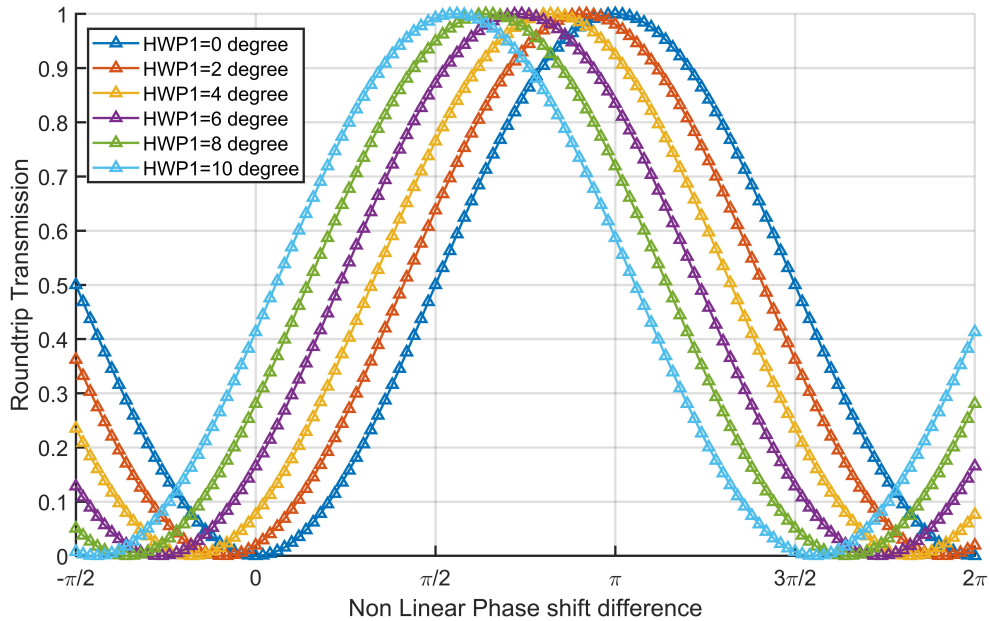


Figure 3.2: Round-trip transmission vs. nonlinear phase shift difference for various orientations of HWP1, with  $\theta_q = \theta_o = 0^\circ$ . Calculated with Eq. (3.3).

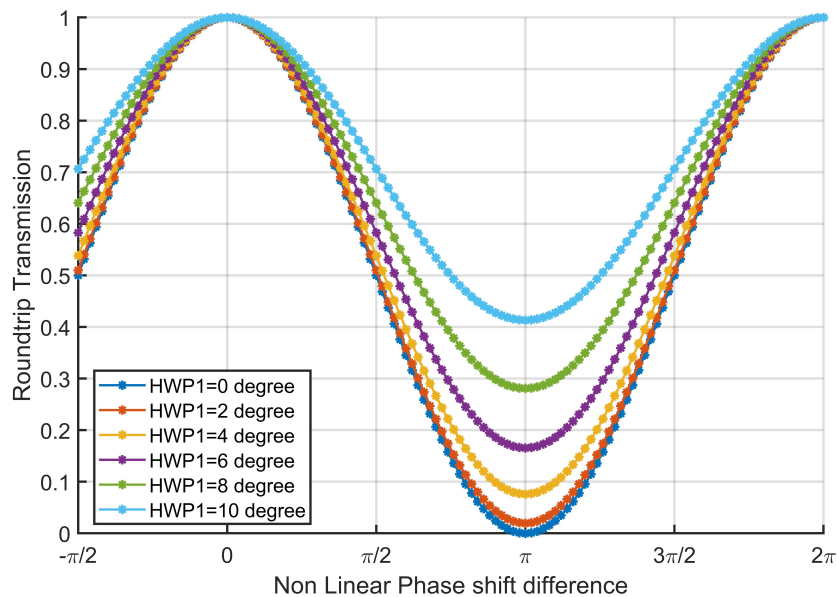


Figure 3.3: Round-trip transmission vs. nonlinear phase shift difference for various orientations of HWP1, with  $\theta_q = 45^\circ$  and  $\theta_o = 0^\circ$ . Calculated with Eq. (3.3).

HWP2 is placed to the left of the PBS, i.e., after the phase-shifted polarization components emerging from the loop have already interfered in the PBS. Therefore, it has no impact on this interference. Rather, this waveplate simply determines what fraction of the light that moves to the left of the PBS gets reflected by the PBS, i.e. the output coupling rate, which is part of the linear loss in the cavity. The impact of rotating HWP2 on the round-trip transmission is shown in Fig. 3.4, where  $\theta_h$  and  $\theta_q$  are kept fixed at  $0^\circ$ . At different HWP2 orientations the transmission is simply scaled by a constant factor between 0 and 1. This output coupling wave plate gives us the ability to adjust the output coupling ratio without affecting the phase bias. Note that, in mode-locked laser operation at a particular nonlinear phase shift difference, the total loss consists of the linear loss (including output coupling loss) and the saturable loss (due to light that left the cavity through the rejection port).

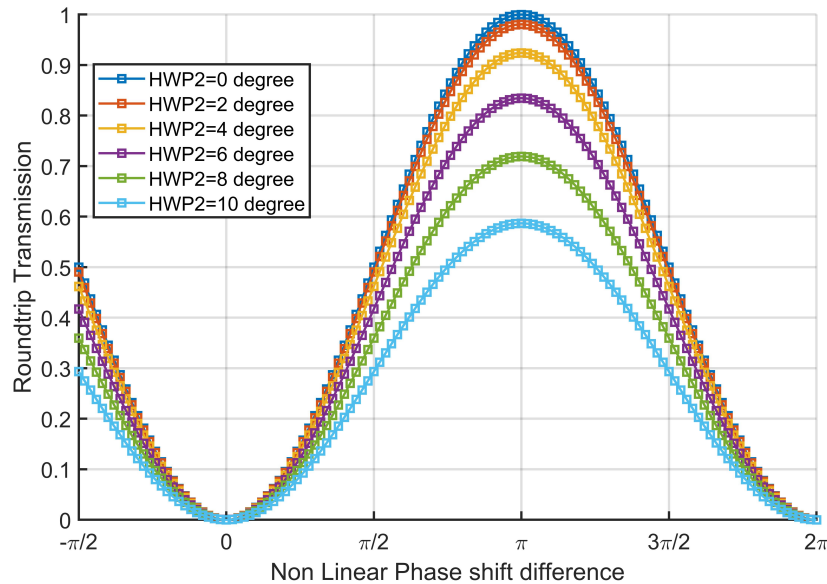


Figure 3.4: Round-trip transmission vs. nonlinear phase shift difference for various orientations of HWP2, with  $\theta_h = \theta_q = 0^\circ$ . Calculated with Eq. (3.3).

### 3.3 Dispersion measurements

This section briefly describes experimental measurements of our laser cavity dispersion. This work was led by my lab mate Saeid Ebrahimzadeh with help from our collaborating group from Vienna.

It has been experimentally established that cavity dispersion has a significant impact on mode-locked laser performance, including noise levels [31]. As mentioned in Section 3.1, having near zero and slightly negative dispersion has been experimentally demonstrated to facilitate low noise operation. Our laser cavity includes a grating pair, where the distance separating the gratings can be used to control dispersion. An initial estimate of the required grating separation can be calculated by adding up the dispersion contribution of each cavity element using vendor data. However, this data is often incomplete (e.g., covers only part of the spectrum) and needs to be extrapolated, leading to increased error. Therefore, we carried out experimental measurements of our laser cavity dispersion.

We characterized our laser cavity dispersion using the method by Knox [42]. In this method, a slit is inserted in a particular portion of the cavity where the optical frequencies are spread out in space. In our laser cavity this specific section is the space in between the end mirror and the grating compressor. To measure the dispersion, at first mode-locked operation is achieved with the slit outside the cavity. Next, the slit is moved laterally across the beam in small steps. Essentially the slit works as a tunable band pass filter. At each step, the laser output optical spectrum and repetition rate,  $f_{rep}$ , are measured. From each measured spectrum we extract the center frequency,  $\omega_c$ , and dispersion values are calculated by post-processing of this data as explained below.

The delay a pulse experiences in one cavity round-trip is, by definition, the group delay of a single round-trip. A time delay Fourier transforms into a spectral phase that depends linearly on frequency, with the delay setting its slope. Therefore, for the frequency dependent

group delay,  $T(\omega_c)$ , we have

$$T(\omega_c) = \frac{\partial\phi}{\partial\omega} = \frac{1}{f_{rep}(\omega_c)}. \quad (3.4)$$

ere,  $\phi$  is the spectral phase accumulated in one round-trip phase. GDD is the dependence of group delay on frequency, i.e.,

$$GDD = \frac{\partial^2\phi}{\partial^2\omega} = \frac{\partial T}{\partial\omega}. \quad (3.5)$$

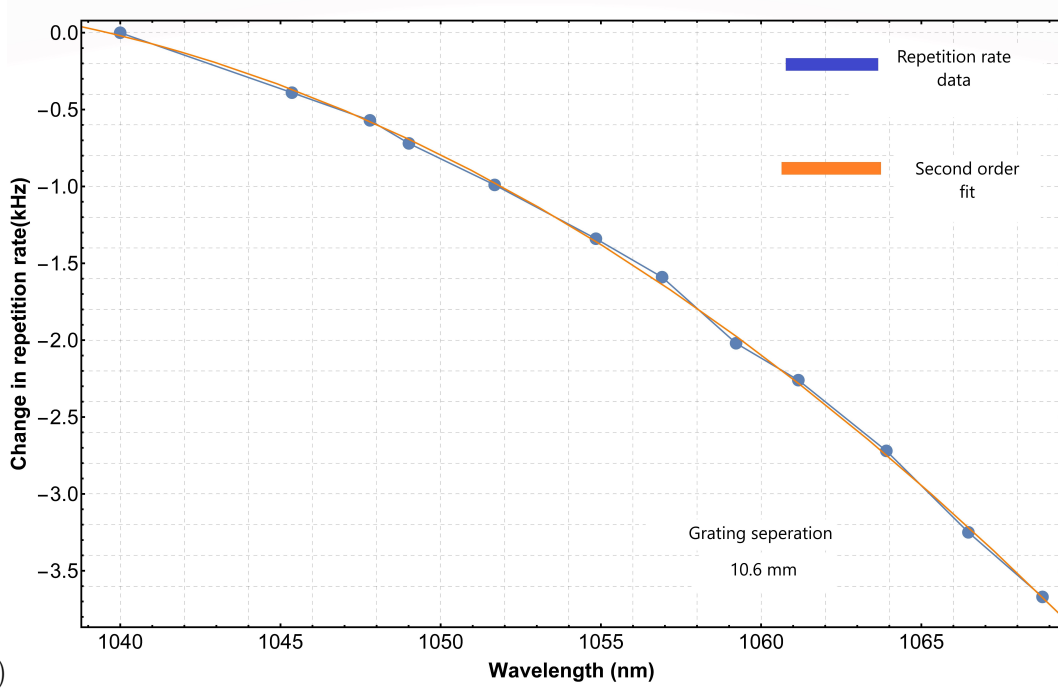
Therefore, in order to obtain the GDD, we fitted  $T(\omega_c)$  to a second order polynomial, and extracted the GDD from its second derivative.

In our experiment, the repetition rate was measured by using an amplified photodiode (New Focus 1601, 1 GHz bandwidth) connected to a frequency counter (Agilent 53230A), and the optical spectrum was recorded with a spectrometer (Aurora 4000). The wave plates orientation angles were  $\theta_q = 70^\circ$ ,  $\theta_h = 35^\circ$  and  $\theta_o = 2^\circ$ . The grating separation was 10.6 mm. The curve shown in Fig. 3.5 (a) was calculated from the fit of delay to frequency. The horizontal axis in this plot is the central wavelength of the recorded spectrum,  $\lambda_c = \frac{2\pi c}{\omega_c}$ .

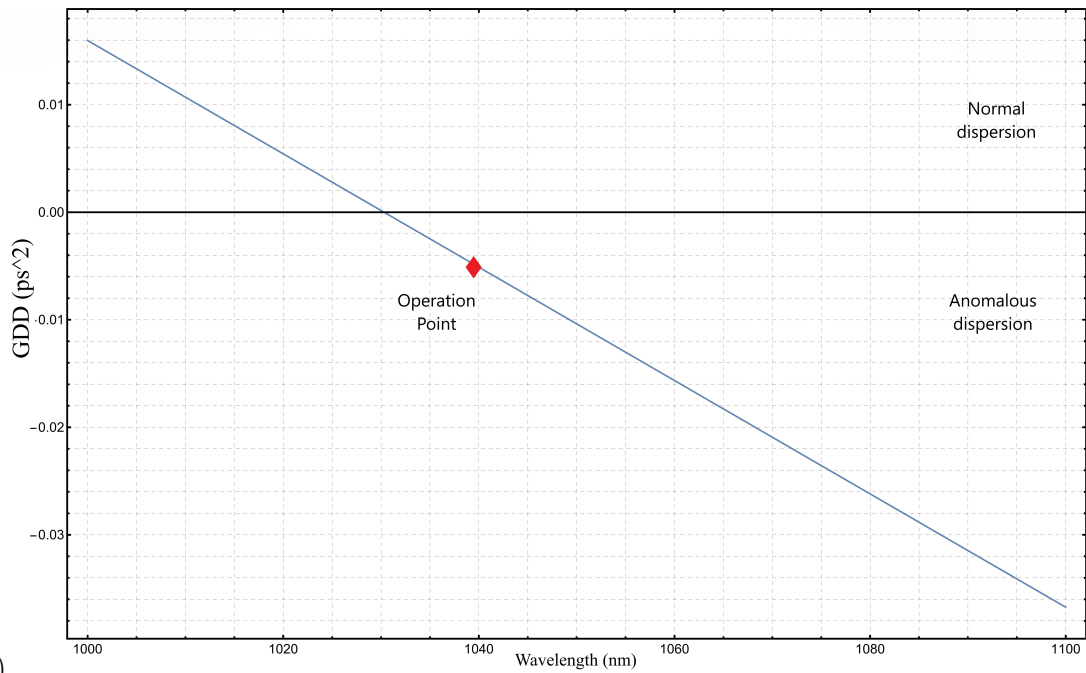
Fig. 3.5 (b) shows the GDD values extracted from the fitted experimental data. The red marker indicates the center wavelength of 1039 nm, which corresponds to operation with the slit out of the cavity, where the net GDD is  $-0.0043 \text{ ps}^2$ . This is indeed a very small and slightly anomalous value. By “small” we mean that this net GDD is much smaller in magnitude than the magnitudes of positive and negative GDD the pulse experiences in the cavity. For example, the only cavity element contributing negative GDD is the grating pair, and its calculated round-trip contribution to GDD is  $-0.015 \text{ ps}^2$ .

Fig. 3.5 (c) shows the experimentally recorded spectra for the various slit positions. The blue curve that peaks at 1039 nm corresponds to having the slit out o the cavity. The vertical line indicates the extracted wavelength at which dispersion is zero, 1030.31 nm. At wavelengths shorter (longer) than this value, dispersion is normal (anomalous). This plot further illustrates how close to zero dispersion our laser operates. While the spectral peak and most of the spectral energy are in the anomalous dispersion regime, a small portion of

the spectrum is in the normal dispersion regime. This is a common situation in dispersion managed mode-locked lasers.



(a)



(b)

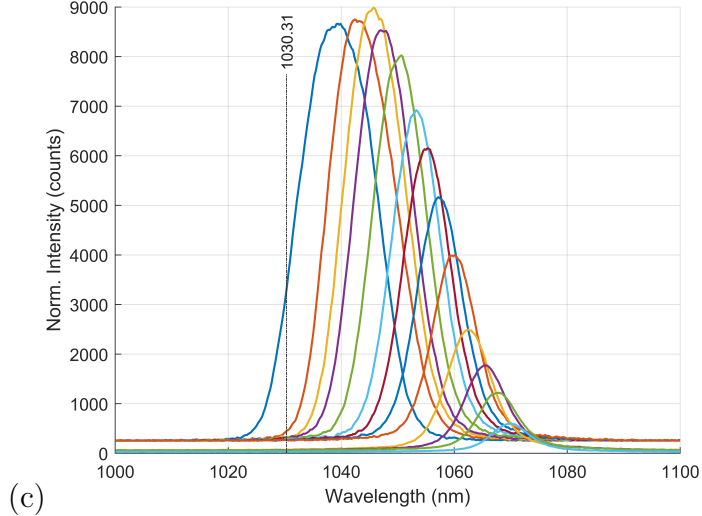


Figure 3.5: (a) Change in pulse repetition rate vs. central wavelength. (b) GDD values extracted from the measurement (see text for details) (c) Optical spectra recorded for various slit positions. The vertical line indicates the extracted zero dispersion wavelength.

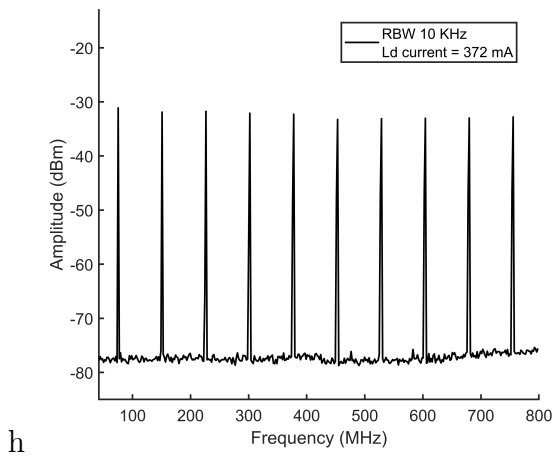
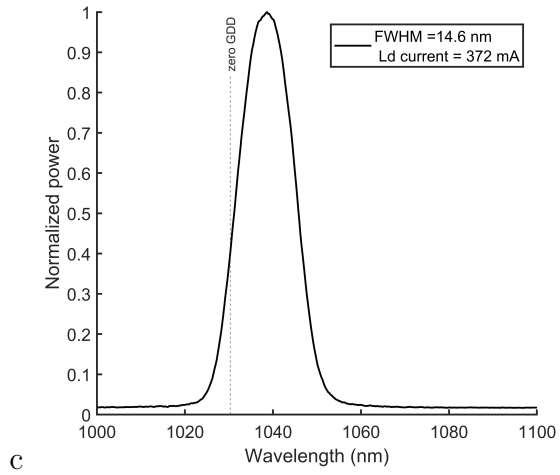
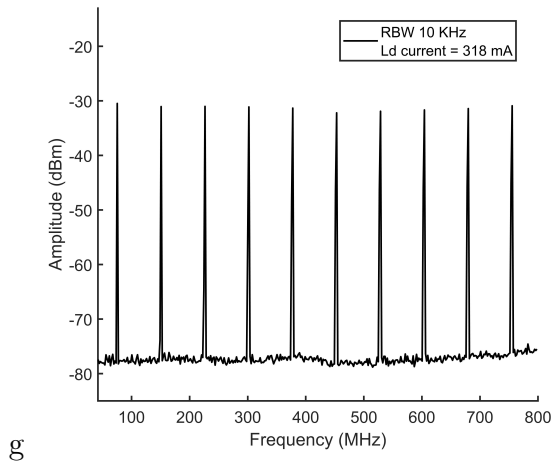
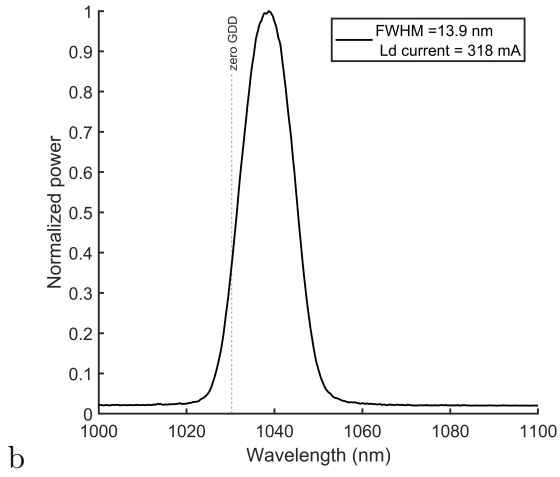
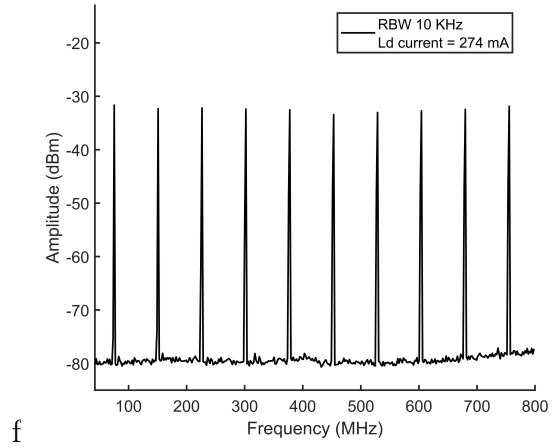
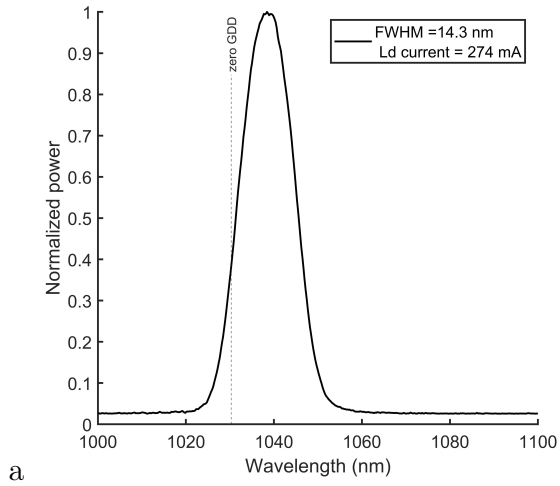
To be clear, in all of the experiments reported in the remainder of this thesis, the grating separation was kept at 10.6 mm.

### 3.4 Mode-locked states characterization

This section shows experimentally measured optical and RF spectra, taken under the same experimental conditions that are used in following sections. These spectra show that under all experimental conditions the laser remained in a stable mode-locked state with near zero and slightly anomalous dispersion.

The orientations of the wave plates in the laser cavity were set to  $\theta_q = 70^\circ$ ,  $\theta_h = 35^\circ$  and  $\theta_o = 2^\circ$ . The grating separation was kept at 10.6 mm, as in Section 3.3. The laser was mode-locked with a pump current of 300 mA. Next, the wave plates were rotated to  $\theta_q = 79^\circ$ ,  $\theta_h = 40^\circ$  and  $\theta_o = 3^\circ$ . The reason for this rotation is explained in the following section). Followingly, the pump diode laser's current was varied from 274 mA to 475 mA and the optical and RF spectra were recorded for each current. In this range of currents the

laser remained stably mode-locked. Lower currents resulted in CW breakthrough (where the laser simultaneously supports both a mode-locked pulse train and a CW lasing component) and higher currents caused double-pulsing (manifested as fringes in the optical and/or RF spectrum). The optical and RF spectra were recorded with an Aurora 4000 GE 200-1100 spectrometer (1 nm resolution) and a Newport 1601 photodetector connected to an Agilent E4401 RF spectrum analyzer (10 kHz RBW), respectively. We note that, throughout the measurement, the laser was boxed to shield against air currents, and care was taken to avoid introducing external vibration to the optical table.



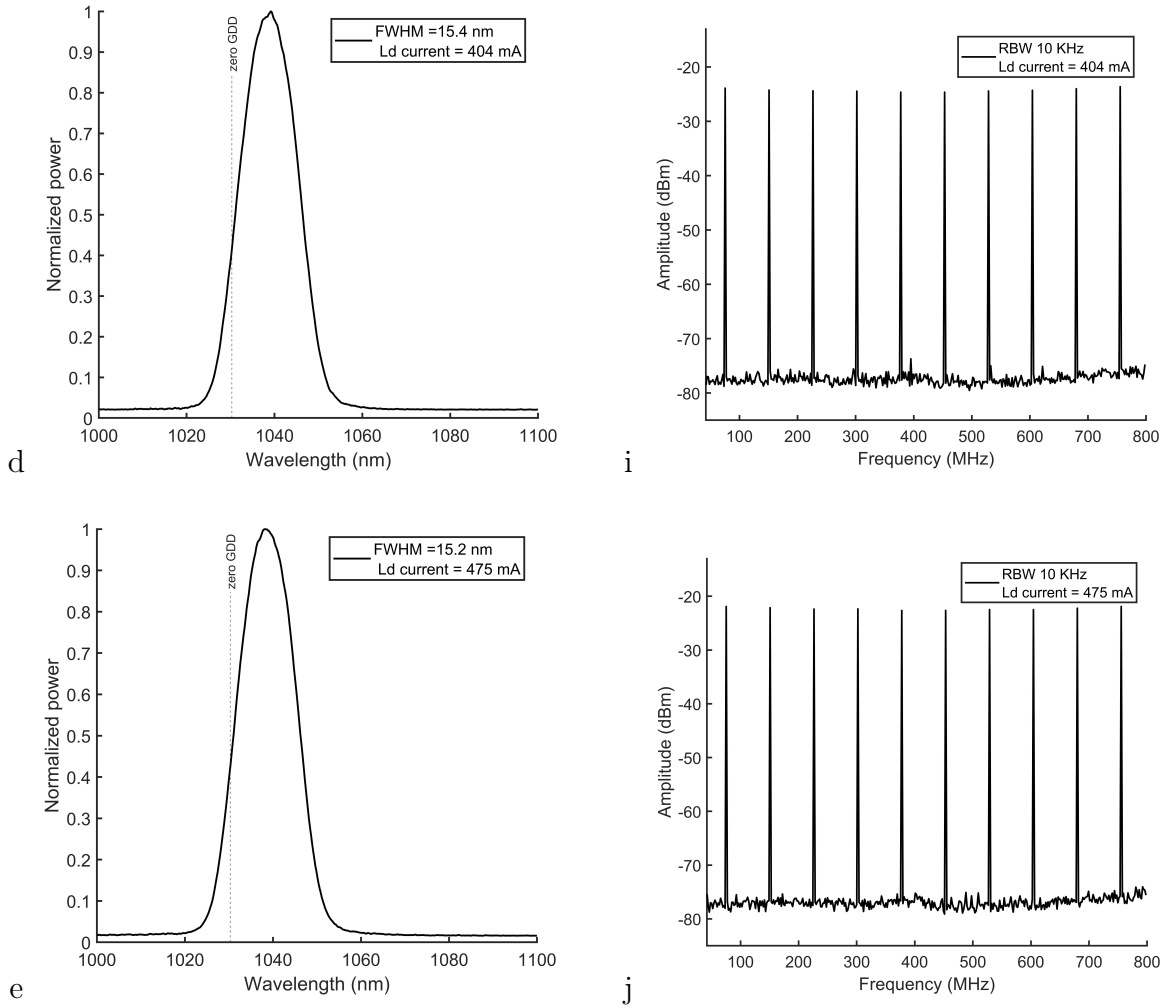


Figure 3.6: (a-e) Optical spectra at different pump currents. The dashed line indicates the wavelength at which the intracavity GDD is zero. (f-j) Corresponding RF spectra. In (a-j), the pump current is indicated in the legend. In (a-e), the legend shows the spectral FWHM.

Fig. 3.6 shows the optical and RF spectra obtained at different pump currents. The optical spectra are all centered at 1039 nm and have very similar shape. In all cases the laser operates in the same near zero and slightly anomalous dispersion regime (see the zero GDD indicator in Figs. 3.6(a-e)). The smooth spectral shape, with no peaks or fringes, corresponds to a stable mode-locked state and contains no evidence of CW breakthrough or multi-pulsing phenomena. The RF spectra in Figs. 3.6 (f-j) consists of peaks at the 75.515 MHz repetition rate and its harmonics, resulting from the pulse train beating against

itself in the photodetector (as explained in Section 2.3.2). In all cases, the peaks at the 10 measured harmonics have nearly identical magnitude, and their width is limited by the instrument's RBW of 10 kHz. Furthermore, they reach at least 45 dB above the noise floor. These features shows that, in all cases, the laser is in a stable mode-locked state with low jitter (see Section 3.5.5 for more details on jitter).

We note that additional measurements, not presented here, were taken with a pump current of 284 mA. At this current the laser exhibited anomalous behavior. These results are presented and discussed in Section 4.6. These measurements are also excluded from the remainder of this chapter.

## **3.5 Intensity noise characterization and suppression**

### **3.5.1 Literature review of intensity noise performance and suppression in mode-locked fiber lasers**

It is very difficult to carry out an all-encompassing study of intensity noise in mode-locked fiber lasers. The reason is that this noise depends on both external sources, mainly the pump noise, as well as the specifics of each and every laser. These include not only the mode-locking mechanism, gain medium and cavity dispersion, but also specific technical details such as alignment and splice loss, which are difficult to measure and control. Finally, RIN at different frequencies results from different sources (e.g., acoustic noise can cause increased intensity noise at acoustic frequencies). At this point, to the best of our knowledge, there is no comprehensive theory that explains how intensity noise depends on all laser properties. Therefore, here we provide an overview of the theory and systematic experimental studies that are currently available.

In Section 2.4 we explained how gain saturation and SAT combine to stabilize the mode-locked pulse train. This mechanism damps out intensity fluctuations, i.e., it suppresses intensity noise. This has been established both theoretically and experimentally [29, 30, 33,

34, 35]. However, the description of the SAT parameter is heuristic and not directly connected to physical parameters. Moreover, SAT could result from a combination of physical processes, e.g., dispersive wave generation and roll-over of the APM mechanism. This suggests that, through SAT, intensity noise depends on the pulse forming mechanism and the dispersion regime, though there is no quantitative model for this dependence. In dispersion managed lasers, experimental studies have found that the lowest RIN is obtained when the net GDD is close to zero and slightly anomalous [37, 38].

A recently published review put together RIN data from 32 studies of low-RIN mode-locked lasers based a wide range of technologies, including solid state and fiber lasers with various real and artificial saturable absorbers [37]. More recently, our collaborators [8], who are using the same laser design as we are (though with different fiber lengths), were able to achieve RIN of -125, -132 and -151 dBc/Hz at 100 Hz, 1 kHz and 100 kHz, respectively. We choose these three frequencies as points of comparison with other lasers, since they are usually much below, near and much above the relaxation oscillation frequency. We note that they were using their laser in a self-starting mode-locked state - the significance of this fact is discussed in Section 3.5.3. Fig. 3.7 presents a few representative sets of RIN data collected from various low-RIN mode-locked lasers spanning a good fraction of the technological landscape. The data in Fig. 3.7(a) is from our collaborators' laser [8]. Fig. 3.7(b) shows RIN for different dispersion regimes from a dispersion-managed NPE Yb: fiber laser [51]. Fig. 3.7(c) presents RIN measured from two co-doped Er:Yb:glass solid-state lasers mode-locked using a SESAM [52]. These lasers are nominally identical, yet still have slightly different RIN performance, due to the difficulty in controlling laser parameters with high precision. The three lasers of Figs 3.7(a-c) have similar RIN performance: about -120 to -130 dBc/Hz at 100 Hz and 1 kHz, and about -150 to -155 dBc/Hz at 100 kHz and higher. Finally, Fig. 3.7(d) shows RIN achieved by active noise suppression in a Yb: fiber laser [32]. This is a so-called similariton laser: it contains a SESAM for initializing mode-locking and operates with net normal dispersion, resulting in significant intracavity chirping and spectral

broadening due to SPM. The latter is limited by an intracavity element (fiber Bragg grating) that provides both negative dispersion and spectral filtering, and thereby facilitates SAT. An electronic system monitors the RIN at the laser output and feeds-back onto the pump current in order to suppress the output RIN. In this case, RIN is kept at about -145 dBc/Hz over 100 Hz to 100 kHz, but increases sharply for higher frequencies due to the limited bandwidth of the electronic feedback system.

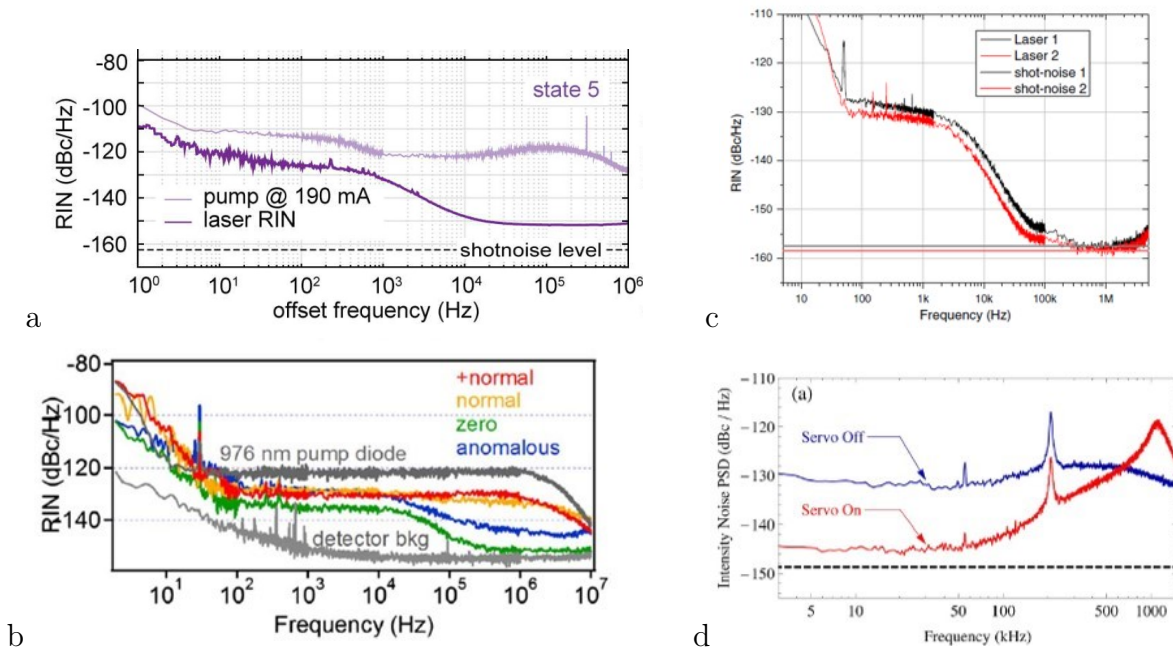


Figure 3.7: Examples of low RIN obtained from mode-locked lasers. (a) All-PM phase-biased NALM Yb: fiber laser, reprinted with permission from [8]. (b) NPE Yb: fiber laser, reprinted with permission from [51], (c) SESAM Er:Yb:glass laser, reprinted with permission from [52], (d) Active intensity noise suppression of a SESAM Yb: fiber similariton laser, reprinted with permission from [32].

In order to provide a broad overview, Table 3.3 shows the range of RIN values obtained at the three representative frequencies. The middle column corresponds to the data from the publications referenced above in this section. For comparison, the right column contains RIN values we achieved with a novel RIN suppression mechanism, as detailed in Sections 3.5.2 and 3.5.3. As the table shows, at 100 Hz and 1 kHz, we have achieved RIN values that are 11 dB lower than any previously published value, to the best of our knowledge.

Additionally, at 100 kHz, our laser is on par with the best published result. Finally, we note that our RIN measurements were limited by background noise in our detector, therefore it is possible that our laser produces even lower RIN than we could measure.

Frequency	RIN (dBc/Hz) (from literature)	RIN (dBc/Hz) (our result)
100 Hz	-110 to -145	-156
1 KHz	-110 to -145	-156
100 KHz	-120 to -155	-156

Table 3.3: Summary of experimentally measured RIN at frequencies that are usually much below, near or much above the relaxation oscillation frequency. The middle column shows the range of values we collected in our literature review. For comparison, the right column shows the RIN values obtained from our laser (see Sections 3.5.2 and 3.5.3 for details).

### 3.5.2 Relative intensity noise measurements

The RIN PSD measurement setup is depicted schematically in Fig. 3.8. The laser’s output port or rejection port beams were detected using an amplified photodetector (New Focus 1801, 125 MHz bandwidth). The photodetector’s output was connected to a home made DC block consisting of a 10 mF capacitor. The DC block’s output was connected to a software defined receiver operating as a real-time RF spectrum analyzer (Signal Hound SA44B). With the analyzer’s input impedance of 50 Ohm, the cut-off frequency of the DC block was 0.32 Hz. The purpose of including the DC block was to prevent damage to the analyzer as per the vendor’s warning. For measuring the photodetector’s average output voltage (i.e., DC voltage), which is proportional to the laser average power, we connected the photodetector directly to a multimeter. The wave plates orientation and grating separation were the same as in Section 3.4. At all times, the laser was boxed up.

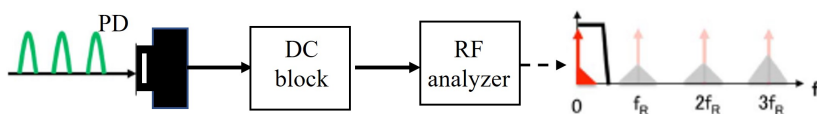


Figure 3.8: Schematic diagram for RIN measurement. Reprinted with permission from [6]

RIN PSD were obtained from the ratio between the photodetector voltage noise PSD

(proportional to the PSD of the square of the laser power),  $S_v(f)$ , and the square of the photodetector DC voltage (proportional to the square of the average laser power),  $V_0^2$ , i.e.,  $S_{RIN} = S_v(f)/V_0^2$  (see Section 2.3.1). Fig. 3.9 shows the obtained RIN PSD at different pump currents, together with the detector's background noise level. These results clearly show that the output port RIN decreased as pump current increased. When going from 274 mA to 475 mA, RIN decreased by at least 20 dB for frequencies below 100 kHz. This reduction is at least 25 dB over the 10 Hz - 10 kHz frequency range. Note that the measurement at 475 mA is limited by the detector background, so the reduction in RIN may be even greater. Furthermore, for frequencies in the range 100 Hz - 100 kHz, the RIN reached an extremely low level of -156 dBc/Hz, limited by the detector background. A comparison of this RIN performance with other published works is given in Section 3.5.1. Overall, these results constitute a demonstration of passive RIN suppression, which is further analyzed below.

The rejection port RIN exhibited a different behavior than the output power RIN. The rejection port RIN significantly exceeds the output port RIN at all pump currents except 318 mA. As the pump current increases, the rejection port RIN experiences a small reduction: from the lowest to the highest current, it decreases by no more than 10 dB at any given frequency. Even at the highest current, where the rejection port RIN is lowest, it remains at least 25 dB higher than the output port RIN for frequencies 10 Hz - 10 kHz.

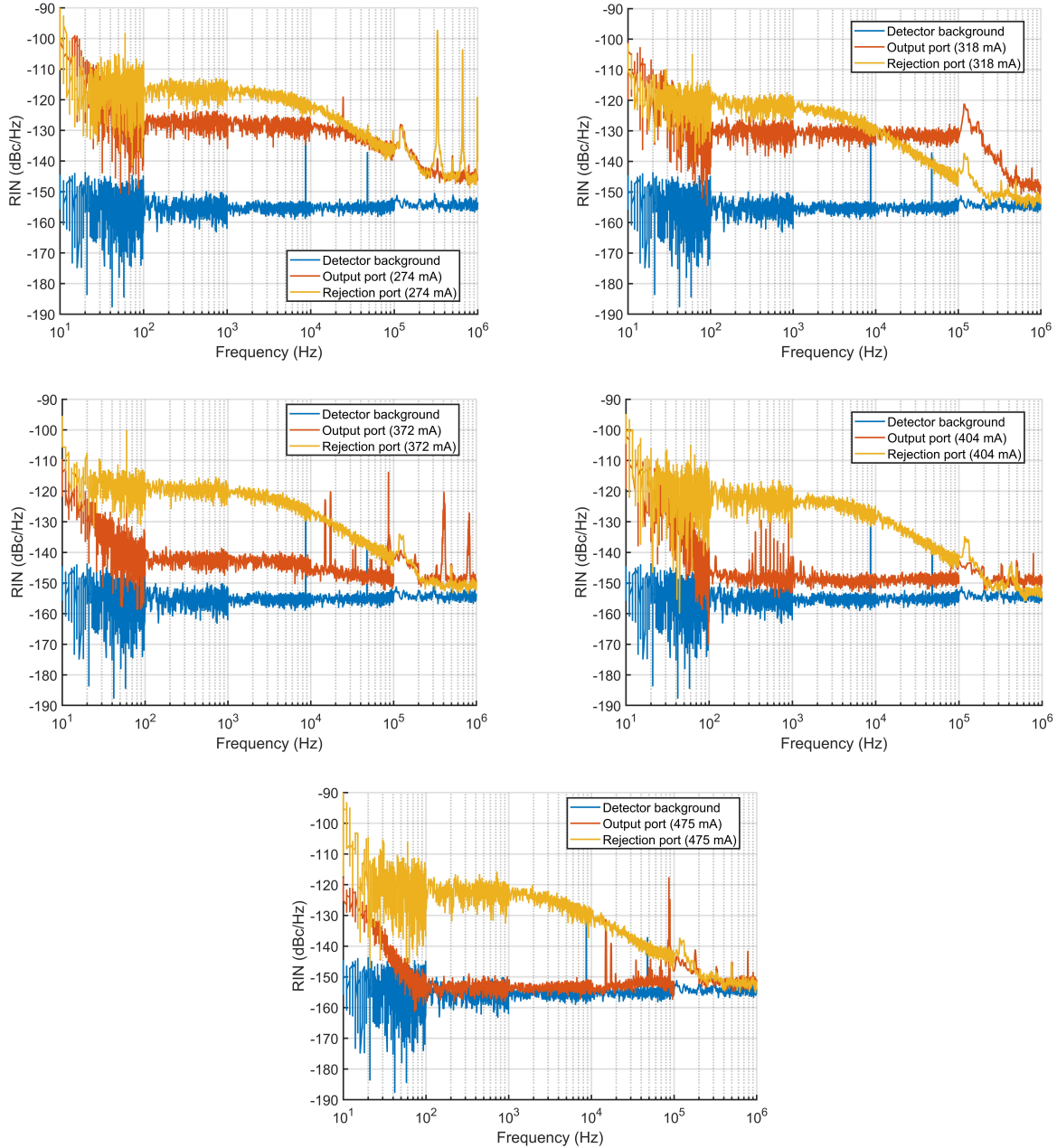


Figure 3.9: RIN PSD measured at different pump currents (indicated in the legends in parentheses) for the laser output port and rejection port. The detector background noise level is also shown.

### 3.5.3 RIN suppression analysis for the mode-locked fiber laser

In Section 3.3 we have shown that our laser operates in the regime of near zero and slightly anomalous dispersion. As explained in Section 2.1, such lasers do not form exact soliton

pulses, but rather pulses that stretch and compress periodically over a cavity round trip. However, by averaging over a cavity round trip, dynamics that are similar to soliton formation emerge. Therefore, in the analysis of our experimental results, we will use the average soliton picture as a way to obtain insight more easily than with a full description of pulse dynamics.

In a soliton mode-locked laser, any optical energy that doesn't fit into the GVD-SPM balance gets transferred from the soliton to the dispersive wave (explained in Section 2.1). For example, if the soliton's amplitude is perturbed, then the perturbation will get transferred to the dispersive wave. In this manner, dispersive wave generation acts to stabilize the soliton. In fact, it is a mechanism of SAT [35]. Since intensity noise constitutes such perturbation, dispersive wave generation acts to suppress intensity noise in the soliton. This mechanism of noise transfer from the soliton to the dispersive wave has been demonstrated experimentally [48].

In the previous section we presented experimental measurements showing output RIN reduction with increasing pump power. We explain these observations partly based on the soliton-to-dispersive wave noise transfer, as well as other possible SAT processes, in addition to a novel mechanism implemented in our laser. The rate of energy transfer from the perturbed soliton to the dispersive wave increases with pulse energy [33]. As pump power increases, so does pulse energy, resulting in a higher rate of noise transfer to the dispersive wave and a reduction in the pulse train's RIN. Other SAT processes (e.g., the roll-over of the transfer function at sufficiently high intensity) also work to stabilize the pulse and thereby reduce RIN in a manner that scales with pulse energy (see Section 2.4).

The additional and novel RIN suppression mechanism in our laser is based on preventing the noisy intracavity dispersive wave from reaching the output port. Fig. 3.10 shows the calculated round trip transmission, transmission to the output port and transmission to the rejection port, as a function of the nonlinear phase shift difference, for the wave plates orientations we used. For a nonlinear phase shift difference near zero, corresponding to low intensity, the transmission to the rejection port is very high while the transmission to the

output is very low. Since the noisy dispersive wave has very low intensity (as explained in Section 2.1), it is transmitted to the rejection port while its transmission to the output port is strongly suppressed. This mechanism enhances RIN suppression in the output port. Overall, as pump power increases, so does the pulse energy, leading to greater transfer of noise from the pulse to the dispersive wave. The latter is prevented from reaching the output port, resulting in the strong reduction in output port RIN presented in the previous section. At the same time, the RIN in the rejection port remains high, since that is where the noisy dispersive wave ends up. Finally, we note that the transmission to the output port of any other low-intensity noisy light, such as amplified spontaneous emission coming from the gain fiber, is also suppressed, further contributing to reduction in output RIN.

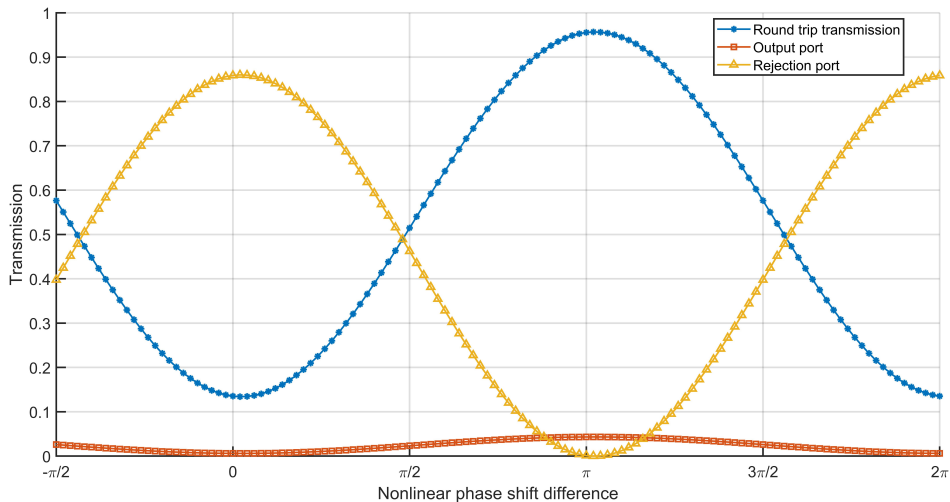


Figure 3.10: Calculated round trip transmission, transmission to the output port and transmission to the rejection port, as a function of the nonlinear phase shift difference. The wave plates orientations are  $\theta_q = 79^\circ$ ,  $\theta_h = 40^\circ$  and  $\theta_o = 3^\circ$ .

As explained in Section 3.4, the laser was first mode-locked with the wave plates orientations at  $\theta_q = 70^\circ$ ,  $\theta_h = 35^\circ$  and  $\theta_o = 2^\circ$ , and only after it was mode-locked the wave plates were rotated to the orientations that produce the transmission curves shown in Fig. 3.10, where RIN suppression is observed. It was not practical to initiate mode-locking directly in the RIN-suppressed configuration. The reason is that, in this case, the round trip trans-

mission has a weak dependence on the nonlinear phase shift difference where this difference is close to zero. In other words, the round trip transmission had a weak dependence on intensity for low intensity. This is not a coincidence. The transmission to the output port is proportional to the round trip transmission by a factor determined with the outcoupling wave plate orientation,  $\theta_0$ . By design, in the RIN-suppressed state, the transmission to the output port has a minimum near zero nonlinear phase shift difference. Therefore, the round trip transmission also has a minimum there, resulting in a weak dependence on intensity for low intensity. The robustness and flexibility of our laser's design make it possible to mode-lock it in a self-starting state and keep it mode-locked as the cavity parameters are varied significantly, thereby getting the advantage of the low RIN state even when this state cannot be reached by self-starting mode-locking. This is a novelty, as past fiber laser designs lack the degrees of freedom necessary to make such controllable variation in cavity parameters, the robustness required to maintain mode-locking under such variation, or both.

In order to further support our claim regarding the significance of the non-self-starting state for achieving low RIN, we measured the RIN in the self-starting state for various pump currents (this set of data was taken by Saeid Ebrahimzadeh). Fig. 3.11(a) shows the calculated transmission curves for this state. Near zero nonlinear phase shift difference, the round trip transmission has a strong positive slope, as required to self-starting mode-locking, and the transmission to the output port is significantly higher than its minimum value. Both of these features are in contrast to the behavior exhibited by the RIN-suppressed state in Fig. 3.10.

Fig. 3.11(b) shows the output port RIN of the self-starting state for various pump currents. The lowest RIN was obtained with a pump current of 350 mA, and it was significantly higher (at least 20 dB for all frequencies) than the lowest RIN obtained for the RIN-suppressed state. Additionally, a further increase of the pump current to 380 mA resulted in higher RIN, whereas the RIN-suppressed state had the opposite trend. These results indicate that the mechanism that prevents low intensity noise from getting transferred to

the output port plays an important role, as RIN reduction cannot be achieved by increasing pump power alone.

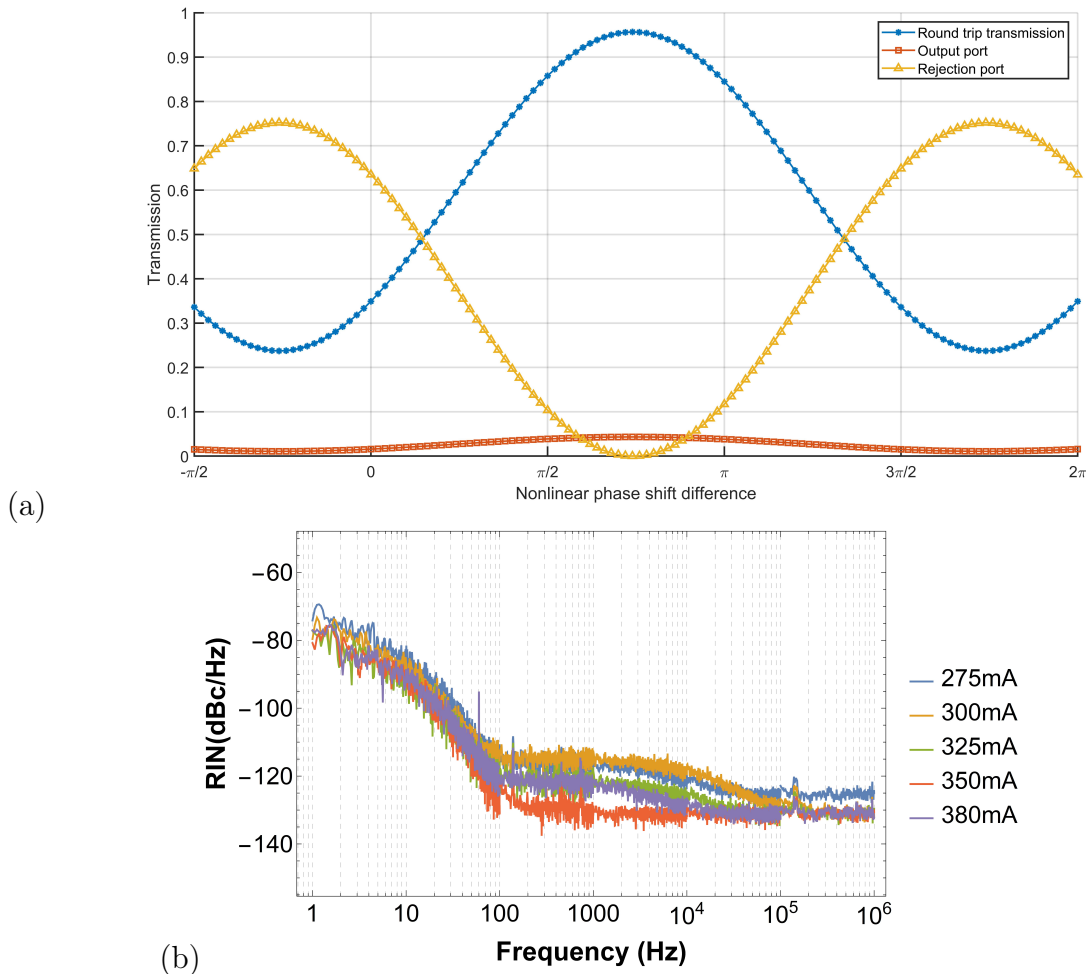


Figure 3.11: (a) Calculated round trip transmission, transmission to the output port and transmission to the rejection port, as a function of the nonlinear phase shift difference. The wave plates orientations are  $\theta_q = 70^\circ$ ,  $\theta_h = 35^\circ$  and  $\theta_o = 2^\circ$ . (b) Output port RIN measured at different pump currents with the same wave plates orientations (taken by Saeid Ebrahimzadeh).

Finally, since mode-locked fiber laser RIN is commonly dominated by pump noise, we need to eliminate the possibility that the reduction in RIN comes from a reduction in pump noise as the pump power increases. We measured the noise of a pump diode of the same make and model that we used for our laser. These measurements are detailed in Appendix A and they show that the pump noise is non-decreasing as the pump current increases from

200 mA to 600 mA, which covers our entire range of pump currents. Therefore, variation in pump RIN cannot be responsible for the observed suppression of RIN at the laser output.

### **3.5.4 Supporting evidence of RIN suppression mechanism theory: output port and rejection port power**

The output port and rejection port power were recorded at different pump currents using a free-space power meter. The results are shown in Fig. 3.12. As the pump current increases from 274 mA to 500 mA the output port power generally increases as well. Starting from 10 mW, the output port power reaches 17 mW at the highest pump current. This generally increasing trend is overlaid with a small dip of about 15% at a pump current of 340 mA. At the same time, the rejection port power shows a much stronger dependence on pump current, increasing from 15 mW to 52 mW over the entire range of currents. Again, this generally increasing trend contains one drop of about 15% at a pump current of 372 mA. Here we remind the reader that additional results showing anomalous behavior are excluded and presented in Section 4.6.

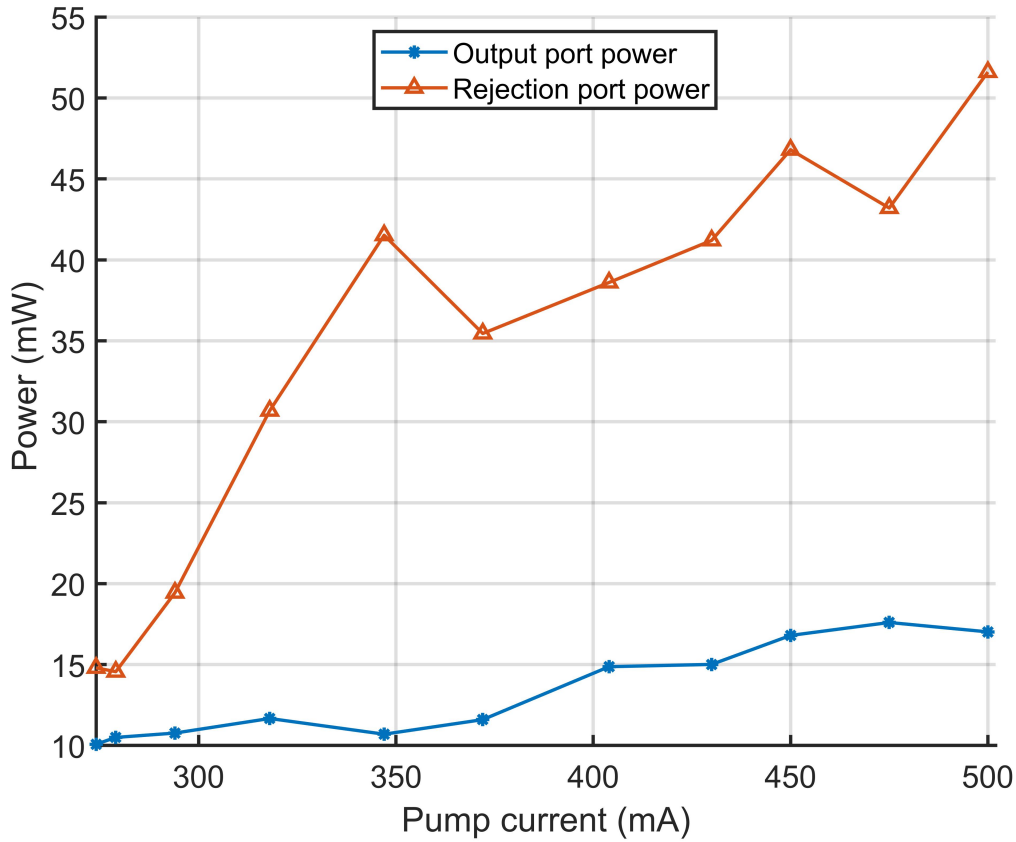


Figure 3.12: Output and rejection port power data for different pump current of laser. The plot shows the power measurement where the pump current is varied from (274~512 mA) and all other setting (i.e. waveplate, grating separation) of the oscillator was similar.

These results fit within the framework of our theoretical explanation of our RIN measurements as follows. As explained in the previous section, low intensity light is emitted through the rejection port while a fraction of the high intensity light (i.e. pulsed light) is coupled out of the cavity through the output port. Fig. 3.12 shows that, as pump power increase, intracavity pulse power experiences a moderate increase while low intensity light increases significantly. The moderate increase in pulse energy leads to stronger SAT and therefore lower pulse RIN, regardless of the physical mechanism that facilitates SAT (dispersive wave generation and/or roll-over of the intracavity transmission). As pulse energy increases, energy transfer from the pulse to the dispersive wave increases, resulting in higher power in the dispersive wave. This noisy low-intensity light is emitted through the rejection port,

contributing to the significantly increased power there. Another possible noisy low-intensity contributor to the rejection port power is ASE. Overall, the combination of moderate increase in pulse power, strong increase in rejected light power and reduction in RIN, as pump power increases, corresponds perfectly to expectations from our theory.

### 3.5.5 Qualitative estimation of timing jitter trend

This section presents experimental evidence qualitatively showing that jitter in our laser improves together with RIN, i.e., as pump power increases. In order to characterize jitter in accordance with the theory presented in Section 2.3.2, we measured the RF spectrum of the 11th harmonic of the laser's repetition rate, where jitter is expected to dominate the PSD. This measurement was carried out with an amplified photodiode (New Focus 1601, 1 GHz bandwidth) and a software defined receiver operating as a real-time RF spectrum analyzer (Signal Hound SA44B). The center frequency in the RF spectrum measurement was set at 830.228478 MHz, the span was 5 KHz and the RBW was 5 Hz. The measurement was done for different pump currents (274 mA to 475 mA) to observe how the change in pump current affects jitter.

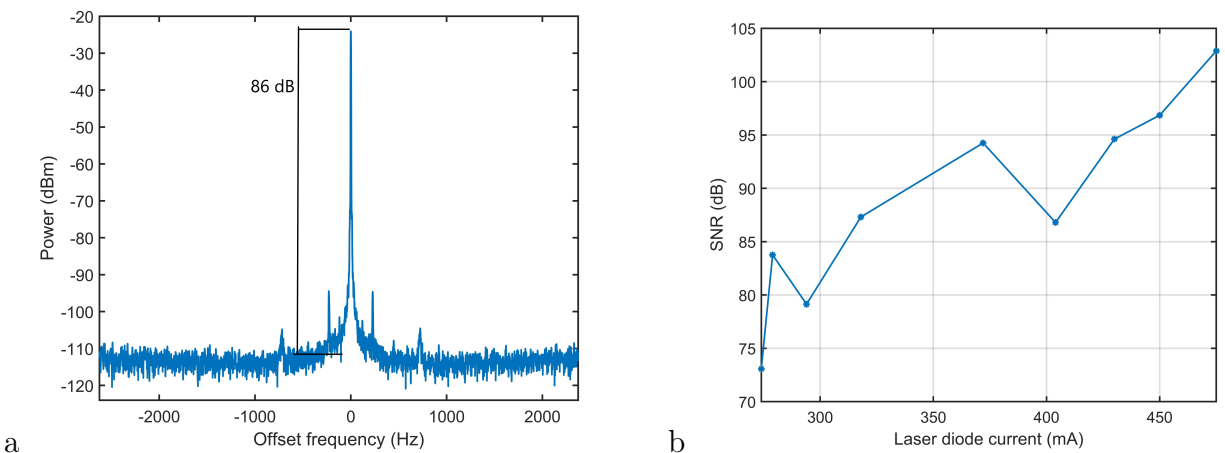


Figure 3.13: (a) Represents the one of the reading (pump current 372 mA) where the SNR was measured for 11th harmonics of the mode-locked laser, (b) Trend of the SNR with the change in pump current, here it can be visible for higher pump current the SNR is increasing and the laser is moving towards a more stable state.

Fig. 3.13 (a) shows an example of one measurement, where the pump current was 372 mA, and a signal to noise ratio (SNR) of 86 dB was obtained. Recall that a higher SNR corresponds to lower jitter. Fig. 3.13 (b) shows SNR measured for the various pump currents, showing a general trend of increasing SNR with increasing pump currents. As the current increases from 274 mA to 475 mA, SNR increases from 73 dB to 103 dB. In addition to the generally increasing trend, there are two dips, at 295 mA and 400 mA, where the SNR drops by 5 and 8 dB, respectively.

The apparent reduction in jitter as pump power increases is correlated with the corresponding reduction in RIN. This correlation may result from intensity noise contribution to the SNR observed here, since in our laser most likely RIN and jitter are coupled through nonlinear effects (and not independent as assumed in the theory in section 2.3.2).

Overall, our laser shows high SNR, corresponding to stable low-noise operation. For comparison, our collaborators have achieved around 95 dB as the best SNR for the same kind of laser but operated in a self-starting state [8], while our laser reaches 103 dB.

## Chapter 4

# Pump-to-output transfer function and anomalous dynamics

Mode-locked fiber lasers can be stabilized through feedback to the pump power. The laser itself is then part of the feedback system, and the bandwidth of its response to variation in pump power limits the feedback bandwidth. An in-depth understanding of the laser mechanisms and their role in determining the feedback bandwidth is important for frequency comb stabilization. It also provides insight into the rich nonlinear dynamics of the mode-locked laser. In this chapter, a perturbation theory approach [30] is summarized and applied to our laser. We establish a relation between SAT and adjustable laser parameters such as waveplates orientations and pump current. We achieve this by assuming that the APM mechanism dominates SAM and SAT. Then, we use our analytical expression for the round trip transmission, Eq. (3.3), to express different parameters of Haus’s master equation (including SAM and SAT) with the cavity “tuning knobs”, i.e, the waveplates orientations. This analysis helps us understand how the “tuning knobs” of the laser can affect different parameters of mode-locking. We also derive a qualitative relationship between the pump-to-output transfer function bandwidth, pump power and waveplates orientations. Afterwards, we present experimental measurements of our laser’s transfer function bandwidth and com-

pare them with our theoretical analysis. Finally, we report on experimental results showing anomalous dynamics in our laser, and we leave the explanation of this phenomenon as a matter for future work.

## 4.1 Modified master equation

In order to simplify the analysis, we assume that dispersion and SPM perfectly compensate for each other (i.e., ideal soliton conditions), so they drop out of the master equation, Eq. (2.9). The remaining terms make up the modified master equation:

$$T_r \frac{da}{dT} = (g - l)a(T) + \gamma_{SAM} a^2(T) + V(a). \quad (4.1)$$

In this section we provide models for gain saturation and SAT and introduce them into the master equation. This is the first step towards making a connection between the parameters of the master equation and the waveplate orientations in our laser.

As explained in Section 2.4, gain dynamics play an important role in mode-locked laser dynamics. Therefore, we begin by describing a simple model for gain saturation in Yb: fiber [29, 30]. This model assumes a 3 level system lasing near resonance. We define the normalized signal power,  $P'_s$ , and normalized pump power,  $P'_P$ , as

$$P'_s = \frac{P_s}{P_{S,SAT}} \quad (4.2)$$

$$P'_P = \frac{P_P}{P_{P,SAT}}. \quad (4.3)$$

Here,  $P_s$  is the signal power and  $P_P$  is the pump power.  $P_{S,SAT}$  is the signal saturation power and  $P_{P,SAT}$  is the pump saturation power. The gain is then given by

$$g = g_0 \left( \frac{P'_P - 1}{1 + P'_P + 2P'_s} \right), \quad (4.4)$$

where  $g_0$  is a constant. The perturbation term, denoted  $V(a)$  in Eq. (4.1), will give rise to shifts in the pulse energy, the phase shift per pulse, the carrier frequency, the round-trip time, and the pulse chirp. Generally, there are many different perturbation sources, such as length fluctuations, gain fluctuations, loss fluctuations, the Raman effect, self-steepening, third-order dispersion, and SAT:

$$V(a) = V_{length} + V_{gain} + \dots + V_{SAT}. \quad (4.5)$$

In our analysis, we are only taking into consideration the perturbation due to SAT. In other words, we are modeling SAT as a perturbation of a stable mode-locked state. We follow [29] to model the SAT perturbation using a power law:

$$V(a) = V_{SAT} = -\gamma_{sat}a^4a(T). \quad (4.6)$$

Here,  $\gamma_{sat}$  is the coefficient for saturation of self amplitude modulation. Substituting this into Eq. (4.1) we have

$$T_r \frac{da}{dT} = (g - l)a(T) + \gamma_{SAM}a^2a(T) - \gamma_{sat}a^4a(T). \quad (4.7)$$

Finally, we introduce the gain saturation model of Eq. 4.4 and obtain

$$T_r \frac{da}{dT} = \left\{ g_0 \left( \frac{P'_P - 1}{1 + P'_P + 2P'_s} \right) - l \right\} a(T) + \gamma_{SAM}a^2a(T) - \gamma_{sat}a^4a(T). \quad (4.8)$$

Since the wave plates orientations control only loss and not gain, in the next section we use Eq. (4.7) to derive analytical expressions that relate  $\gamma_{SAM}, \gamma_{sat}$  and  $l$  to these orientations. Gain saturation is reintroduced later, in Section 4.3.

## 4.2 Derivation of analytical expressions for loss, self-amplitude modulation and its saturation

The pulse envelope,  $a(t)$ , is normalized such that the pulse energy,  $w$ , is given by

$$w = \int |a(t)|^2 dt. \quad (4.9)$$

Substituting this relation into Eq. 4.7 produces an equation for the pulse energy dynamics,

$$T_r d_T w = 2w[(g - l) + \alpha_1 \gamma_{SAM} A^2 - \alpha_2 \gamma_{sat} A^4]. \quad (4.10)$$

Here,  $\alpha_1 = \frac{2}{3}$  and  $\alpha_2 = \frac{8}{15}$  are constants and  $A$  is the pulse's peak amplitude [30]. Next, we assume the laser operates under ideal soliton conditions. This is not true for our laser, which is a dispersion managed laser. However, dispersion managed lasers do have many similarities with soliton lasers, such as a closed relationship between pulse amplitude, pulse duration, and laser cavity parameters [33, 34, 35]. Therefore, we make this assumption to simplify our analysis and progress towards understanding the connection between the Haus model and physical parameters, albeit qualitatively. For a soliton of pulse duration  $\tau$ , in a medium with dispersion parameter  $D$  and SPM coefficient  $\delta$ , we have [30]

$$A\tau = \sqrt{\frac{2|D|}{\delta}}. \quad (4.11)$$

Since  $\tau^{-1} \sim \omega_{rms}$ , where  $\omega_{rms}$  is the pulse's root mean square bandwidth, we can write the approximate relation

$$A \sim \tau^{-1} \sim \omega_{rms} \sim w, \quad (4.12)$$

where we used Eq. (4.11) and the last step stems immediately from Parseval's theorem for a soliton pulse (which has an envelope  $a(t) \propto \text{sech}(t/\tau)$ ).

The evolution of the pulse energy can be expressed using the round trip transmission

(RTT),  $T_{RTT}$ :

$$w(T + T_r) = w(T) T_{RTT}(w). \quad (4.13)$$

For convenience, we recast our analytical expression for the RTT, Eq. (3.3), in the form

$$T_{RTT}(w) = \beta_{1wp}(\cos(\varphi_{nl} - b)) + \beta_{2wp} \quad (4.14)$$

where  $\varphi_{nl}$  is the nonlinear phase shift difference and the parameters  $\beta_{1wp}$  and  $\beta_{2wp}$  depend on the waveplates orientations. We can now rewrite Eq. (4.13) as

$$w(T + T_r) = w(T) \{ \beta_{1wp}(\cos(\varphi_{nl} - b)) + \beta_{2wp} \}. \quad (4.15)$$

In our laser, the nonlinear phase shift difference is the difference between the nonlinear phase shifts of the waves counter propagating in the fiber loop,

$$\varphi_{nl} = \varphi_{nl}^a - \varphi_{nl}^b. \quad (4.16)$$

Since  $\varphi_{nl} \propto I$  (see Eq. (1.1)) and  $I \propto A^2$ , and according to Eq. (4.12)  $A \propto w$ , we have  $\varphi_{nl} \propto A^2 \propto w^2$ . We then define a parameter,  $\kappa$ , such that

$$\varphi_{nl} = \kappa w^2. \quad (4.17)$$

We substitute this into Eq. (4.15) and get

$$w(T + T_r) = w(T) \{ \beta_{1wp}(\cos(\kappa w^2 - b)) + \beta_{2wp} \}. \quad (4.18)$$

Using trigonometric identities, we bring Eq. (3.3) to the form of Eq. (4.14). By comparing

them we get expressions for the waveplate-dependent parameters of Eq. (4.14):

$$\beta_{1wp} = \frac{\cos^2(4\theta_o)}{8} \left\{ [(4\sin^2(2\theta_q) + \{\sin(4\theta_h) - \sin(4\theta_q - 4\theta_h)\})^2 - 4\cos^2(4\theta_h - 2\theta_q)]^2 + [4(\sin(4\theta_h) - \sin(4\theta_q - 4\theta_h)) \cos(4\theta_h - 2\theta_q)]^2 \right\}^{1/2} \quad (4.19)$$

$$\beta_{2wp} = \frac{1}{4} \cos^2(4\theta_o) \left\{ \frac{\{4\sin^2(2\theta_q) + \{\sin(4\theta_h) - \sin(4\theta_q - 4\theta_h)\}^2\}}{2} + 2\cos^2(4\theta_h - 2\theta_q) \right\} \quad (4.20)$$

$$b = \tan^{-1} \left( \frac{4\{\sin(4\theta_h) - \sin(4\theta_q - 4\theta_h)\} \cos(4\theta_h - 2\theta_q)}{4\sin^2(2\theta_q) + \{\sin(4\theta_h) - \sin(4\theta_q - 4\theta_h)\}^2 - 4\cos^2(4\theta_h - 2\theta_q)} \right). \quad (4.21)$$

We now have an expression for the dependence of the pulse energy evolution over one period on the waveplates orientations. Recall that, in the previous section, we modeled SAT as a power law perturbation. In order to express this perturbation using the waveplate orientations, we now use a Taylor expansion to approximate the cosine energy dependence of Eq. (4.18) as a power series and simplify the expression:

$$w(T + T_r) \approx w(T) T_{RTT}(w) \approx w(T) \left[ (\beta_{1wp} + \beta_{2wp}) - \frac{1}{2} \beta_{1wp} (\kappa w^2 - b)^2 \right] \quad (4.22)$$

$$= w(T) \left[ (\beta_{1wp} + \beta_{2wp}) - \frac{1}{2} \beta_{1wp} (\kappa^2 w^4 - 2\kappa w^2 b + b^2) \right] \quad (4.23)$$

$$= w(T) \left[ (\beta_{1wp} + \beta_{2wp}) - \frac{1}{2} \beta_{1wp} \kappa^2 w^4 + \beta_{1wp} \kappa w^2 b - \frac{1}{2} \beta_{1wp} b^2 \right]. \quad (4.24)$$

After some regrouping we have

$$w(T + T_r) \approx w(T) T_{RTT}(w) = w(T) \left[ (\beta_{1wp} + \beta_{2wp} - \frac{1}{2}\beta_{1wp}b^2) + \beta_{1wp}\kappa w^2b - \frac{1}{2}\beta_{1wp}\kappa^2 w^4 \right]. \quad (4.25)$$

Note that the above approximation means that we assume that the laser operates near the peak of the transmission function (where the cosine term equals 1). This is a reasonable assumption, since that region corresponds to stable operation.

In the derivation of the master equation, Haus assumed that the cavity components apply only small perturbations in a single round trip (see Section 2.2). We apply the same assumption to the round trip variation in energy:

$$w(T + T_r) \approx w(T) + T_r d_T w. \quad (4.26)$$

By comparing eq. (4.25) and eq. (4.26) we get

$$w(T) + T_r d_T w = w(T) \left[ (\beta_{1wp} + \beta_{2wp} - \frac{1}{2}\beta_{1wp}b^2) + \beta_{1wp}\kappa w^2b - \frac{1}{2}\beta_{1wp}\kappa^2 w^4 \right]. \quad (4.27)$$

We use this expression for the term  $T_r d_T w$  in Eq. (4.10) and obtain

$$w(T) + 2w[(g-l) + \alpha_1 \gamma_{SAM} A^2 - \alpha_2 \gamma_{sat} A^4] = w(T) \left[ (\beta_{1wp} + \beta_{2wp} - \frac{1}{2}\beta_{1wp}b^2) + \beta_{1wp}\kappa w^2b - \frac{1}{2}\beta_{1wp}\kappa^2 w^4 \right]. \quad (4.28)$$

Next, we use the approximation relation of Eq. (4.12) between the peak amplitude and pulse energy,

$$2w[(g-l) + \alpha_1 \gamma_{SAM} w^2 - \alpha_2 \gamma_{sat} w^4] = w(T) \left[ (\beta_{1wp} + \beta_{2wp} - 1 - \frac{1}{2}\beta_{1wp}b^2) + \beta_{1wp}\kappa w^2b - \frac{1}{2}\beta_{1wp}\kappa^2 w^4 \right], \quad (4.29)$$

and rearrange to get

$$2[(g-l)+\alpha_1\gamma_{SAM}w^2-\alpha_2\gamma_{sat}w^4] = \left[ (\beta_{1wp} + \beta_{2wp} - (1 + \frac{1}{2}\beta_{1wp}b^2)) + \beta_{1wp}\kappa w^2b - \frac{1}{2}\beta_{1wp}\kappa^2w^4 \right]. \quad (4.30)$$

Finally, we equate the coefficients of powers of energy on both sides of the equation. This gives us expressions for the SAM and SAT parameters in terms of the waveplates orientations (contained in  $\beta_{1wp}$ ):

$$\gamma_{SAM} = \frac{1}{2} \frac{\beta_{1wp}}{\alpha_1} \kappa b \quad (4.31)$$

$$\gamma_{sat} = \frac{1}{4} \frac{\beta_{1wp}}{\alpha_2} \kappa^2. \quad (4.32)$$

The energy-independent part of the right hand side of Eq. (4.30) expresses the non-saturable loss,  $l$ :

$$l = \frac{1}{2} \left[ (1 + \frac{1}{2}\beta_{1wp}b^2) - (\beta_{1wp} + \beta_{2wp}) \right]. \quad (4.33)$$

Now that we have analytical expressions for the SAM, SAT and loss parameters from the master equation, we can investigate how they depend on the intracavity waveplates orientations. This is done in the next section.

### 4.3 nonlinear loss and pump-to-output transfer function bandwidth

At this point, we have four gain and loss parameters:  $g$ ,  $\gamma_{SAM}$ ,  $\gamma_{sat}$  and  $l$ . Before we proceed, we will incorporate three of these parameters, namely  $g$ ,  $\gamma_{SAT}$  and  $l$ , into a single parameter called the nonlinear loss, thus simplifying the remainder of the analysis. This is the same nonlinear loss parameter that was introduced in Section 2.4. Additionally, we can eliminate  $\gamma_{SAM}$  from our expressions. We do this by noting that in steady state the overall gain must equal the overall loss (linear and nonlinear), i.e. the net gain is zero. Introducing this condition into Eq. (4.10) yields a closed relation between  $\gamma_{SAM}$ , gain, loss and the pulse

peak amplitude  $A \sim w$ :

$$g + \alpha_1 \gamma_{SAM} A^2 = l + \alpha_2 \gamma_{sat} A^4. \quad (4.34)$$

Next, we represent a perturbation of the pulse envelope by writing  $a = a_0 + \Delta a$ , where  $a_0 = Asech(t/\tau)$  is the steady state soliton solution that satisfies Eq. 4.34. The corresponding perturbed energy is  $w = w_0 + \Delta w$ . Using Eq. (4.9) we write the energy perturbation as

$$\Delta w = Re \left[ 2 \int a_0 \Delta a dt \right] \quad (4.35)$$

where we kept terms only up to first order in  $\Delta a$ . Finally, we introduce this expression into Eq. (4.7) and obtain the dynamic equation for energy perturbation,

$$T_r d_T \Delta w = -\eta \Delta w, \quad (4.36)$$

where  $\eta$  is the nonlinear loss,

$$\eta = \alpha_3 (g - l) + \alpha_4 \gamma_{sat} w^4, \quad (4.37)$$

and  $\alpha_3 = 4$  and  $\alpha_4 = \frac{32}{15}$  are constants [30]. At this point, we have derived the expression for  $\eta$  that was introduced in Section 2.4. [30].

We now use Eqs. 4.31, 4.32 and 4.33 to write the nonlinear loss as a function of our laser's waveplates orientations,

$$\eta = \alpha_3 \left[ g - \frac{1}{2} \left\{ \left( 1 + \frac{1}{2} \beta_{1wp} b^2 \right) - (\beta_{1wp} + \beta_{2wp}) \right\} \right] + \frac{\alpha_4}{4} \frac{\beta_{1wp}}{\alpha_2} \kappa^2 w^4. \quad (4.38)$$

We use Eq. (4.17) to explicitly show the dependence of  $\eta$  the nonlinear phase shift difference,  $\varphi_{nl}$ :

$$\eta = \alpha_3 \left[ g - \frac{1}{2} \left\{ \left( 1 + \frac{1}{2} \beta_{1wp} b^2 \right) - (\beta_{1wp} + \beta_{2wp}) \right\} \right] + \frac{\alpha_4}{4} \frac{\beta_{1wp}}{\alpha_2} \varphi_{nl}^2. \quad (4.39)$$

Finally, we introduce gain saturation by expressing  $g$  using Eq. (4.4), and also substitute

$\alpha_2 = \frac{8}{15}$ ,  $\alpha_3 = 4$  and  $\alpha_4 = \frac{32}{15}$ :

$$\eta = 4 \left[ g_0 \left( \frac{P'_P - 1}{1 + P'_P + 2P'_S} \right) - \frac{1}{2} \left\{ \left( 1 + \frac{1}{2} \beta_{1wp} b^2 \right) - (\beta_{1wp} + \beta_{2wp}) \right\} \right] + \beta_{1wp} (\varphi_{nl})^2. \quad (4.40)$$

Saturation power is given by  $P_{SAT} = \pi r^2 I_{SAT}$ , where

$$I_{SAT} = \frac{h \frac{c}{\lambda}}{(\sigma_{abs} + \sigma_{em}) \tau} \quad (4.41)$$

and  $I_{SAT}$  is the saturation intensity [54]. Here,  $h$  is Planck's constant,  $\sigma_{abs}$  is the absorption cross section,  $\sigma_{em}$  is the emission cross section and  $\tau$  is the upper state lifetime. For wavelength of 1030 nm, which is close to our laser's central wavelength of 1039 nm, the emission cross section is  $0.8 \times 10^{-24} m^2$  [54], the upper state lifetime 800  $\mu s$ , and the mode field diameter is 3 micron. The saturation power is then  $P_{S,SAT} = 2.13$  mW. For wavelength of 975 nm, which is very close to our pump's wavelength of 976 nm, the absorption cross section is  $2.7 \times 10^{-24} m^2$  [54] and all other parameter are the same as for the laser at 1030 nm.. The saturation power is then  $P_{P,SAT} = 0.67$  mW. We pump our laser with about 100-200 mW of power. Our laser's output power is on the order of 10 mW, and the intracavity power is even higher. Therefore, our laser operates in the strongly saturated regime, i.e.,  $P'_P = \frac{P_P}{P_{P,SAT}} \gg 1$  and  $P'_S = \frac{P_S}{P_{S,SAT}} \gg 1$ . Therefore, Eq. (4.40) can be written as

$$\eta \approx 4 \left[ g_0 \left( \frac{P'_P}{P'_P + 2P'_S} \right) - \frac{1}{2} \left\{ \left( 1 + \frac{1}{2} \beta_{1wp} b^2 \right) - (\beta_{1wp} + \beta_{2wp}) \right\} \right] + \beta_{1wp} (\varphi_{nl})^2. \quad (4.42)$$

For fixed pump power  $P'_P$  will remain constant. However,  $P'_S$  will change according to the waveplates orientations. Therefore we write

$$\eta \approx 4 \left[ g_0 \left( \frac{P'_P}{P'_P + 2 \frac{P_{S,WP}}{P_{S,SAT}}} \right) - \frac{1}{2} \left\{ \left( 1 + \frac{1}{2} \beta_{1wp} b^2 \right) - (\beta_{1wp} + \beta_{2wp}) \right\} \right] + \beta_{1wp} (\varphi_{nl})^2. \quad (4.43)$$

Here,  $g_0$  can be used as a fitting constant.

According to the theory presented in Section 2.4, the bandwidth of the pump-to-output transfer function,  $\nu_{3dB}$ , is determined by

$$\nu_{3dB} = (1 + \eta^{-1})\nu_{3dB}^{gain-medium}, \quad (4.44)$$

where

$$\nu_{3dB}^{gain-medium} = \frac{1}{2\pi T_g} \quad (4.45)$$

is the bandwidth of the gain's response to perturbation, and  $T_g$  is the gain relaxation time. While in practice  $T_g$  depends on pump power, we assume that its variation is small enough to neglect, and then we have simply

$$\nu_{3dB} \propto \left(1 + \frac{1}{\eta}\right), \quad (4.46)$$

which we write as

$$\nu_{3dB} = k\left(1 + \frac{1}{\eta}\right), \quad (4.47)$$

where  $k$  is a constant.

Eqs. (4.43) and (4.47) establish a relationship between the bandwidth of the pump-to-output transfer function, the pump power and the waveplates orientations. Therefore, they can guide the choice of these parameters such that a desired trade-off may be struck between the bandwidth available for stabilization and other considerations such as low output RIN. The next two sections present experimental measurements of  $\nu_{3dB}$  and discuss their agreement with the analysis presented here.

## 4.4 Pump-to-output transfer function bandwidth measurements

In this experiment we record the transfer function between the pump diode laser current to the laser output power. A diagram of the experimental setup is shown in Fig.4.1. This measurement was carried out using a standard swept-sine technique. A signal analyzer (Agilent 89441A) provided a small swept-sine signal for modulating the pump current. The laser output power is detected using a photodiode. The photodiode's output voltage is used as an input to the signal analyzer, which produces the transfer function.

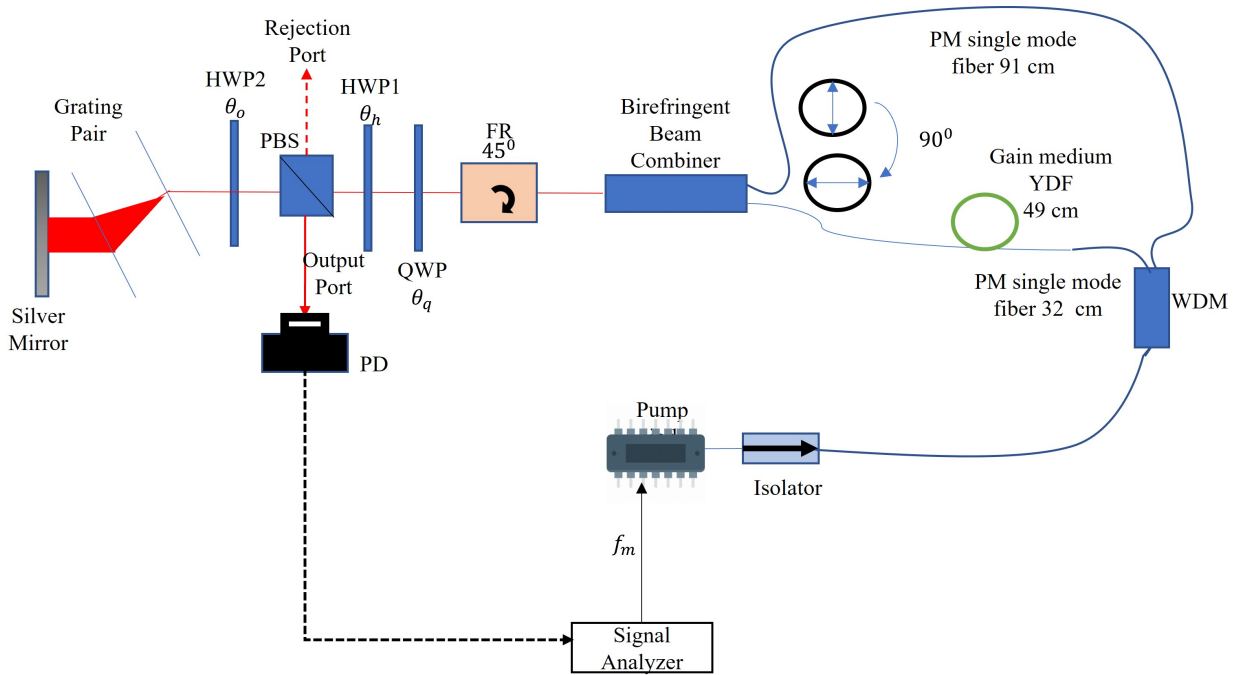


Figure 4.1: Experimental setup for measuring the pump-to-output transfer function of the mode-locked fiber laser.  $f_m$  is the frequency of the pump current modulation signal provided by the signal analyzer. PD: photodiode.

The modulation frequency range was 0 Hz to 1 MHz. In order to maintain good spectral resolution and low noise throughout this range, the measurements were taken with variable spans, RBWs and averaging, as detailed in Table 4.1. In all cases the modulation signal RMS voltage was 5 mV, which the pump laser controller translates into a modulation current of

6.25 mA RMS.

Start Frequency(Hz)	Stop Frequency(Hz)	RBW(Hz)	Average
1e0	1e2	2.0e-1	20
8e1	1e3	2.0e+0	30
8e2	1e4	2.0e+1	100
8e3	1e5	2.0e+2	100
8e4	1e6	2.0e+3	100

Table 4.1: Settings used in experimental measurements of the transfer function.

The transfer functions measured for different pump currents are shown in Fig.4.2. These results were normalized such that they all have a value of 0 dB at a frequency of 10 Hz. Although I have taken transfer function measurements at 11 different pump currents, for the sake of clarity, Fig.4.2 shows only the transfer function measurements that have the same pump currents as our RIN measurement data from section 3.5.2. In Fig. 4.3(a) the complete trend of transfer function bandwidth for 11 pump currents is shown.

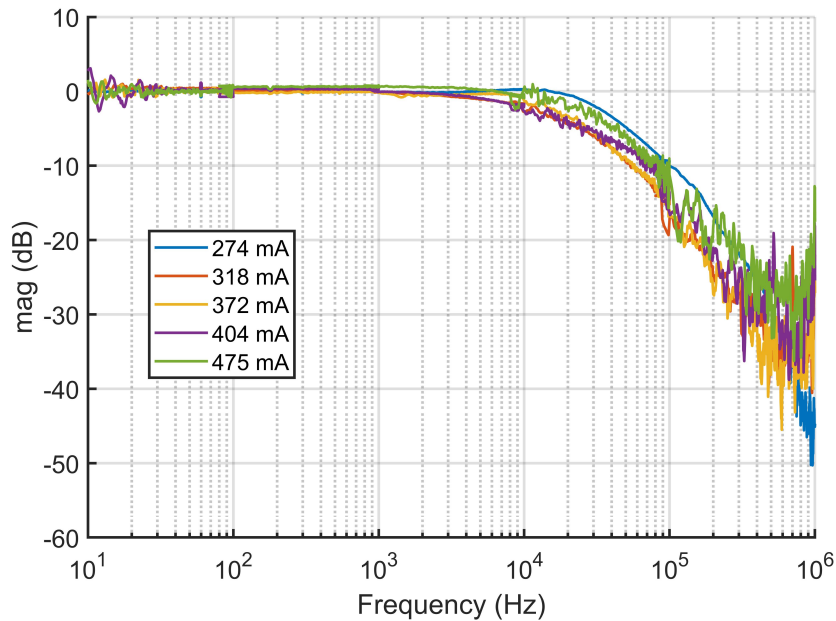


Figure 4.2: Normalized pump-to-output transfer function at different pump currents.

## 4.5 Transfer bandwidth performance analysis

In this section we discuss how the measurement results presented in the previous section compare with the theory developed in the first three sections of this chapter. We also explain how these results are consistent with the experimental dependence of our laser's RIN on pump current, which was presented and analyzed in Section 3.5. Finally, we explain how all of this pertains to a trade-off between stabilization bandwidth and RIN suppression.

Fig. 4.3 shows the 3 dB bandwidth of the pump-to-output transfer function vs. pump current. As pump current increases, the bandwidth has a generally decreasing trend, with some oscillations along the way. Overall, the bandwidth decreases from 41 kHz at 274 mA to 7 kHz at 500 mA. According to Eq. (4.47), this means that the nonlinear loss,  $\eta$ , increases with pump current. This is exactly the behavior we expect from our analytical expression for  $\eta$ , Eq. (4.43). There, not only  $P'_P$ , but also  $\varphi_{nl}$  increases with pump current, since  $\varphi_{nl}$  increases with pulse energy and we've shown experimentally that pulse energy increases with pump current (see Section 3.5.4).

The transfer bandwidth measurement reassembles the stability condition of the laser and also the laser behavior towards the damping of intrinsic fluctuation, a correlation can be found between the transfer bandwidth and RIN behavior. From Fig. 4.2(a) it can be observed that at lower pump current (274 mA) the highest 3dB transfer bandwidth can be correlated to the RIN behavior at 274 mA pump current. Also around 372 mA pump current the 3dB transfer bandwidth gets reduced which means in this particular state by a qualitative manner the nonlinear loss  $\eta$  has higher value than comparing to the laser state at 274 mA pump current. This means by increasing the pump current the laser moves towards a higher stability condition.

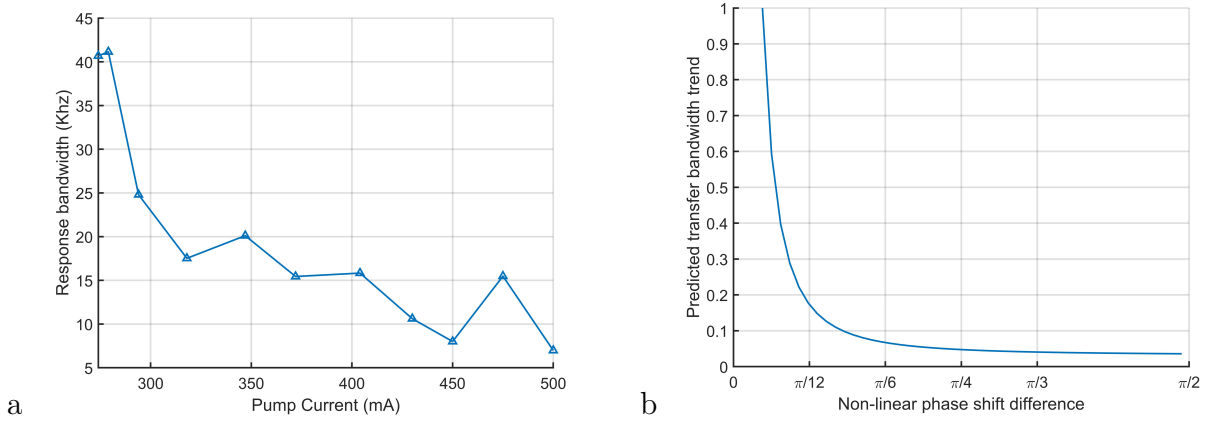


Figure 4.3: (a) 3 dB bandwidth of the pump-to-output transfer function vs. pump current, (b) Theoretically calculated normalized bandwidth of the pump-to-output transfer function as a function of nonlinear phase shift difference.

The increase in  $\eta$  represents an increase in the SAT action, which leads to better stability against perturbation, as explained in Section 2.4. Indeed, in the experimental results presented in Section 3.5, the laser output RIN and jitter decrease with increasing pump current - in correlation with the decreasing bandwidth and increasing  $\eta$ . Fig. 4.3(b) shows the theoretical prediction of the dependence of the bandwidth on the nonlinear phase shift,  $\varphi_{nl}$ , which increases with pump current due to the growing pulse energy. Note that this plot neglects the dependence of  $P'_p$  on pump current, i.e., it implicitly assumes a very strong saturation of the pump transitions, such that  $\frac{P'_p}{P'_p + 2P'_s} \approx 1$  for all pump currents that facilitate mode-locked operation. We see that our theory qualitatively captures the bandwidth's trend of decreasing with increasing pump current.

Overall, we see that increasing the pump current reduces RIN and jitter, while at the same time reducing the bandwidth available for frequency stabilization via pump current. Therefore, a trade-off between these laser properties must be struck according to the requirements of each application. The analytical expressions derived in the first three sections of this chapter provide a guide as to how this trade-off will be affected by pump current and waveplates orientations.

## 4.6 Anomalous dynamics and double pulsing behavior discussion

As mentioned throughout the preceding text, in the process of carrying out experimental measurements we collected data that does not conform to the theory we presented, or any other theoretical model of mode-locked lasers that we are aware of. This section presents these experimental results, which we term anomalous dynamics.

Fig. 4.4 shows data that was collected with the pump current set to 284 mA, which we call the anomalous point. This figure also shows the data obtained with pump current of 512 mA, which shows clear indications of double-pulsing. We include the double-pulsing data in order to contrast it with the anomalous point and show that double-pulsing cannot explain our observations at 284 mA.

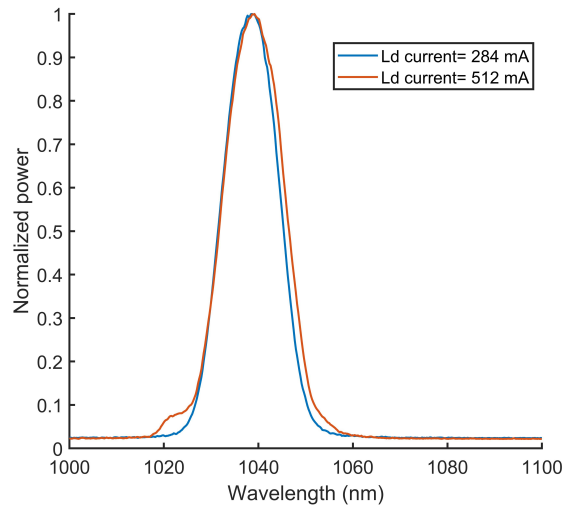
Fig. 4.4(a) presents the optical spectra at the anomalous point and the double-pulsing case. The anomalous point spectrum is very similar to the spectra obtained with pump currents that displayed stable low-noise mode-locked operation (see Fig. 3.6). There is no indication of CW breakthrough or any fringes that might result from multi-pulsing. The spectrum for the double-pulsing state is generally similar, except that it is slightly broader and includes a small bump on its short wavelength side, around 1023 nm.

Fig. 4.4(b) shows the RF spectrum of the lowest 10 harmonics of the repetition rate, for both the anomalous point and the double-pulsing state. Again, the anomalous point spectrum looks very similar to that of stable low-noise mode-locked operation at other pump currents (shown in Fig. 3.6). The spectrum of the double-pulsing state shows a clear signature of double-pulsing: a (partial) fringe pattern, with a minimum at the fourth harmonic (near 300 MHz). This pattern results from the interference of two temporally-shifted pulse train reaching the photodetector.

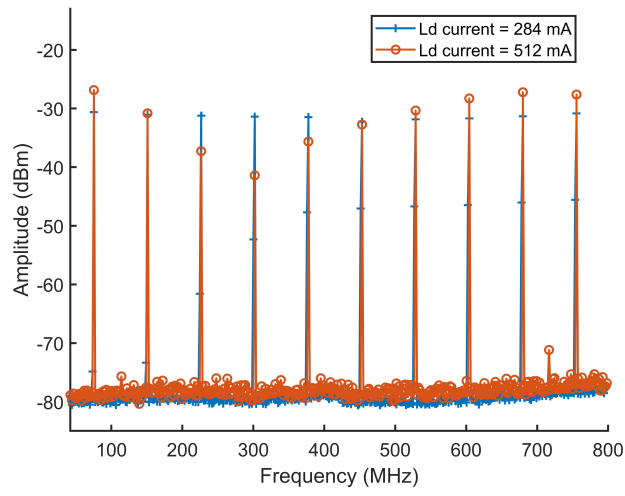
In Fig. 4.4(c) we present the pump-to-output transfer functions for the anomalous point and double-pulsing state. Both cases are different from the results for stable low-noise mode-

locked state, which had a simple roll-off behavior, much like a simple low-pass filter, of about 10 dB/decade (see Fig. 4.2). For both anomalous and double-pulsing state we see a bump in the transfer function, rising 3-5 dB above the low frequency response. For the double-pulsing state, this bump peaks at about 6 kHz and then rolls off at about 10 dB/decade, similarly to the stable mode-locked states of Fig. 4.2. We interpret this bump as a resonance where the responses of the two pulse trains interfere constructively. Outside the resonance each pulse train's response rolls off just like in the stable mode-locked cases. Notably, the double-pulsing data is much noisy. This results from fluctuations in the relative delay between the pulse trains due to their independent jitter noise. The anomalous point shows different behavior. Its bump peaks at a much higher frequency of about 30 kHz and then rolls off much faster, at about 40 dB/decade. It also lacks the noise characteristic of multi-pulsed operation. We note that, while the data presented here was collected from the laser's output port, the anomalous point's pump-to-rejection port transfer function shows the same behavior as its pump-to-output port transfer function.

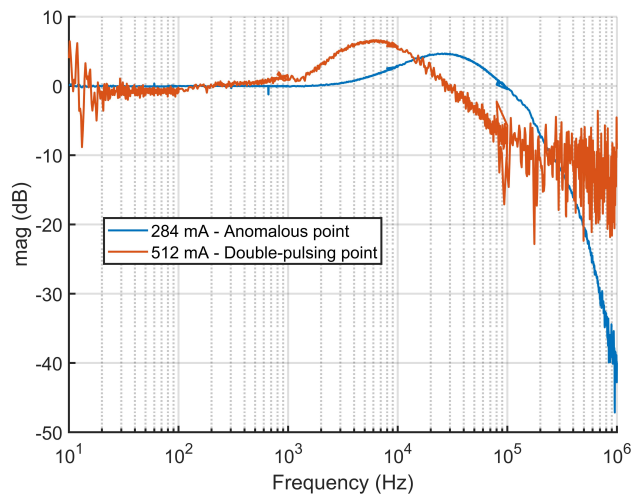
Fig. 4.4(d) shows output port power and rejection port power as a function of pump current. The output port power does not show any variation around the anomalous point or the double-pulsing state. However, the rejection port power has a sharp minimum at the anomalous point. At slightly lower and slightly higher pump currents, the output power is 2-3 times higher, i.e., the drop is by about 50-60%. Notably, at slightly lower or slightly higher pump current the laser recovers its usual stable low-noise mode-locking behavior, with not CW breakthrough or multi-pulsing. We could easily reproduce this phenomenon multiple times and at different days, where the the pump current that corresponds to the minimum in rejection power changed very little from day to day. The output power also drops for the double-pulsing case, where the pump current is increased from 500 mA to 512 mA, but the drop is only about 10%.



a



b



c

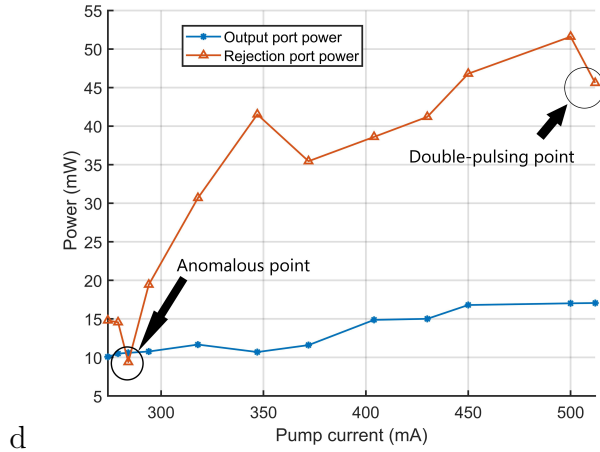


Figure 4.4: Experimental measurements for the the anomalous point (pump current of 284 mA) and double-pulsing state (pump current of 512 mA). (a) Optical spectra. (b) RF spectra. (c) Pump-to-output transfer functions. (d) Output port and rejection port power.

At this point we do not have a solid explanation for this behavior of the laser. A possible explanation is dual relaxation [49]: the relaxation oscillations of the two polarization component in the PM fiber can be delayed with respect to each other. When they interfere constructively the oscillation gets enhanced, and destructive interference leads to much a weaker response to an oscillatory perturbation. This could explain the peak and strong roll-off we observe in the transfer function. Also, this is still single-pulse operation, which corresponds to the observed spectra and the absence of additional noise in the transfer function measurement. However, it is not clear why the rejection port power would show a sharp drop as a result of dual relaxation. Further investigation is required to understand this anomaly, including experiments that could confirm or rule out dual relaxation.

# Chapter 5

## Conclusion

In this thesis, the development and characterization of a flexible, self-starting, and easy to operate all-PM NALM mode-locked fiber laser were demonstrated. A detailed experimental investigation of the laser's performance was presented, including optical and RF spectra, dispersion, intensity noise and timing jitter. The laser has a repetition rate of 75.5MHz, a center wavelength of 1039 nm and a spectral bandwidth of about 15 nm. Among many great qualities of this laser, its self-starting mode-locking behavior is particularly valuable from a practical point of view. With the proper orientation of the intracavity waveplates and appropriate pump current, the laser will mode-lock by itself without any external influence.

The flexibility of the laser comes from a combination of its robustness (due to its all-PM fiber construction) and its different “tuning knobs”, i.e., the three intracavity waveplates orientations, intracavity grating pair, and pump laser power (controlled through the current delivered to it). Two of the waveplates control the phase bias and modulation depth, while the third control the output coupling rate. The grating pair controls the net intracavity dispersion. Pump power controls the mode-locked operating point as determined by the nonlinear phase shift difference between the two wave counter-propagating in the fiber loop.

In-operando dispersion measurement revealed that this dispersion-managed laser works in the near zero and slightly anomalous dispersion regime, known to facilitate low-noise op-

eration. Here, experimental measurements of relative intensity noise showed that, with a certain set of waveplates orientations, noise strongly decreased as pump current increased. An explanation for this passive noise suppression was provided and supported with experimental evidence. Briefly, increasing the pump current transfers more noise from the pulse to a low intensity dispersive wave. The waveplates orientations were chosen such that low intensity light is separated from the laser's output port, and directed towards a different power (called the rejection port). It is possible that other related processes also contribute to our observations, such as the additive pulse mode-locking mechanism itself, as well as the separation of low intensity amplified spontaneous emission from the pulse through the same mechanism that sent the dispersive wave to the rejection port. Overall, we achieved values that, to the best of our knowledge, constitute record low relative intensity noise for a mode-locked fiber laser. This achievement was made possible thanks to the robustness and flexibility of our laser, that made it possible to tweak its tuning knobs while it remains mode-locked. Indeed, the low noise state we achieved is not a self-starting mode-locking state. Rather, the laser needs to be started in a self-starting state and then brought to the low noise state by adjusting the waveplates orientations. A qualitative measurement for timing jitter was also carried out. This investigation showed that the repetition rate beat note SNR at the laser output improved as pump current increased.

This thesis also details the derivation of approximate analytical expressions for parameters from Haus's master equation for mode-locked lasers, as well as the bandwidth of the laser's pump-to-output transfer function. In particular, expressions were derived for the linear loss, self amplitude modulation and saturation of self amplitude modulation parameters, as functions of physical parameters such as pump power and orientation of the intracavity waveplates. This qualitative analysis provides guidance as to the dependence of the laser's mode-locked state on its tuning knobs. Additionally, it helps us understand the trade-off between intensity noise and jitter suppression on the one hand, and the bandwidth of the pump-to-output transfer function on the other hand. This bandwidth is a limiting factor

for active stabilization of the laser frequency (i.e., frequency comb stabilization). Therefore, understanding this trade-off is important in order to choose the best operating conditions for each application. We presented experimental measurements of the bandwidth of the pump-to-output transfer function, which qualitatively agree with our theoretical analysis.

The final section of this thesis discussed experimental observations that do not fit within the theoretical framework we presented, or any other that we know of. These observations were made when the pump current had a certain value. While we do not have a complete understanding of these observations, we proposed a possible explanation: a known phenomenon called double relaxation, where the relaxation oscillations of different polarization components in a PM fiber laser are delayed with respect to each other. Further investigation is necessary in order to confirm or disprove our hypothesis.

In summary, we have demonstrated the development, analysis, and characterization of an all-PM NALM mode-locked laser. With the self-starting and noise suppression capability of this laser, our group is moving towards building a high power frequency comb laser system. This will require active frequency stabilization and chirped-pulse amplification. Indeed, a frequency comb is a stabilized pulsed laser, characterized by very low phase noise. Therefore, any future work on our laser system must include phase noise measurements. Phase noise is known to be strongly correlated with intensity noise in mode-locked fiber lasers, evidently due to nonlinear conversion of intensity noise to phase noise. Therefore, we expect the low intensity noise of our laser to contribute to phase noise reduction. We also note that, while we presented experimental evidence to support our theoretical explanation of our laser's intensity noise suppression mechanism, additional data could strengthen our claim. These include optical spectra of the rejection port light, pump-to-rejection port transfer function, and dependence on waveplates orientations over a wider range of values. The same is true for our analytically derived expressions for the master equation parameters and pump-to-output transfer function bandwidth. Furthermore, these expressions can be made more quantitatively accurate by eliminating some simplifying assumptions we made in their

derivation, e.g., perfect soliton operation. Such investigations will facilitate optimization of laser operation for frequency comb applications with strict noise requirements.

# Bibliography

- [1] S. S. Dhillon et al., “The 2017 terahertz science and technology roadmap,” *J. Phys. D: Appl. Phys.* 50, 043001 (2017).
- [2] Picqué, N., Hänsch, T.W. Frequency comb spectroscopy. *Nature Photon* 13, 146–157 (2019).
- [3] Peter T. C. So, Chen Y. Dong, Barry R. Masters, Keith M. Berland, “Two-Photon Excitation Fluorescence Microscopy,” *Annual Review of Biomedical Engineering* 2, 399-429 (2000).
- [4] Corkum, P., Krausz, F., “Attosecond science,” *Nature Phys* 3, 381–387 (2007).
- [5] Fortier, T. M. et al., “Generation of ultrastable microwaves via optical frequency division,” *Nature Photonics* 5, 425–429 (2011).
- [6] J. Kim and Y. Song, "Ultralow-noise mode-locked fiber lasers and frequency combs: principles, status, and applications," *Adv. Opt. Photonics* 8(3), 465–540 (2016).
- [7] Sugioka, K., Cheng, Y., “Ultrafast lasers—reliable tools for advanced materials processing,” *Light Sci Appl* 3, e149 (2014).
- [8] Aline S. Mayer, Wilfrid Grosinger, Jakob Fellingner, Georg Winkler, Lukas W. Perner, Stefan Droste, Sarper H. Salman, Chen Li, Christoph M. Heyl, Ingmar Hartl, and Oliver H. Heckl, "Flexible all-PM NALM Yb: fiber laser design for frequency comb applications: operation regimes and their noise properties," *Opt. Express* 28, 18946-18968 (2020).

- [9] Hänsel, W., Hoogland, H., Giunta, M. et al. "All polarization-maintaining fiber laser architecture for robust femtosecond pulse generation," *Appl. Phys. B* 123, 41 (2017).
- [10] V. J. Matsas, T. P. Newson, D. J. Richardson, and D. N. Payne, "Selfstarting passively mode-locked fibre ring soliton laser exploiting nonlinear polarisation rotation," *Electron. Lett.* 28(15), 1391–1393 (1992).
- [11] O. Okhotnikov, A. Grudinin, and M. Pessa, "Ultra-fast fibre laser systems based on SESAM technology: New horizons and applications," *New J. Phys.* 6, 1–22 (2004).
- [12] D. Popa, Z. Sun, F. Torrisi, T. Hasan, F. Wang, and A. C. Ferrari, "Sub 200 fs pulse generation from a graphene mode-locked fiber laser," *Appl. Phys. Lett.* 97(20), 203106 (2010).
- [13] Y.-W. Song, S. Yamashita, C. S. Goh, and S. Y. Set, "Carbon nanotube mode lockers with enhanced nonlinearity via evanescent field interaction in D-shaped fibers," *Opt. Lett.* 32(2), 148–150 (2007).
- [14] E.P. Ippen, H.A. Haus, L.Y. Liu, "Additive pulse mode locking., " *J. Opt. Soc. Am. B* 6, 1736–1745 (1989).
- [15] N. J. Doran and D. Wood, "Nonlinear-optical loop mirror," *Opt. Lett.* 13(1), 56–58 (1988).
- [16] M. E. Fermann, F. Haberl, M. Hofer, and H. Hochreiter, "Nonlinear amplifying loop mirror," *Opt. Lett.* 15(13), 752–754 (1990).
- [17] Boyd, Robert W., *Nonlinear optics*. Academic press, 2020.
- [18] J. W. Nicholson and M. Andrejco, "A polarization maintaining, dispersion managed, femtosecond figureeight fiber laser," *Opt. Express* 14(18), 8160–8167 (2006).
- [19] Pupeza, Ioachim, et al. "Extreme-ultraviolet frequency combs for precision metrology and attosecond science," *Nature Photonics* 15, 175-186 (2021).

- [20] Cundiff, Steven T., and Jun Ye. "Colloquium: Femtosecond optical frequency combs," *Reviews of Modern Physics* 75, 325 (2003).
- [21] Y. Ma, B. Xu, H. Ishii, F. Meng, Y. Nakajima, I. Matsushima, T. R. Schibli, Z. Zhang, and K. Minoshima, "Low-noise 750 MHz spaced ytterbium fiber frequency combs," *Opt. Lett.* 43(17), 4136–4139 (2018).
- [22] M. Lezius, T. Wilken, C. Deutsch, M. Giunta, O. Mandel, A. Thaller, V. Schkolnik, M. Schiemangk, A. Dinkelaker, A. Kohfeldt, A. Wicht, M. Krutzik, A. Peters, O. Hellmig, H. Duncker, K. Sengstock, P. Windpassinger, K. Lampmann, T. Hülasing, T. W. Hänsch, and R. Holzwarth, "Space-borne frequency comb metrology," *Optica* 3(12), 1381–1387 (2016).
- [23] M. Baumgartl, C. Lecaplain, A. Hideur, J. Limpert, and A. Tünnermann, "66 W average power from a microjoule-class sub-100 fs fiber oscillator," *Opt. Lett.* 37(10), 1640–1642 (2012).
- [24] W. Liu, H. Shi, J. Cui, C. Xie, Y. Song, C. Wang, and M. Hu, "Single-polarization large-mode-area fiber laser mode-locked with a nonlinear amplifying loop mirror," *Opt. Lett.* 43(12), 2848–2851 (2018).
- [25] F. Li, P. K. A. Wai, and J. N. Kutz, "Geometrical description of the onset of multipulsing in mode-locked laser cavities," *J. Opt. Soc. Am. B* 27(10), 2068–2077 (2010).
- [26] Dian Duan, Jie Wang, Yang Wu, Jindong Ma, and Qinghe Mao, "Approach to high pulse energy emission of the self-starting mode-locked figure-9 fiber laser," *Opt. Express* 28, 33603–33613 (2020).
- [27] H. A. Haus and A. Mecozzi, "Noise of mode-locked lasers," *IEEE J. Quantum Electron.* 29, 983–996 (1993).

- [28] N. Haverkamp, H. Hundertmark, C. Fallnich, and H. R. Telle, "Frequency stabilization of mode-locked Erbium fiber lasers using pump power control," *Appl. Phys. B* 78, 321-324 (2004).
- [29] B. R. Washburn, W. C. Swann, and N. R. Newbury, "Response dynamics of the frequency comb output from a femtosecond fiber laser," *Opt. Express* 13, 10622-10633 (2005).
- [30] N. R. Newbury and B. R. Washburn, "Theory of the frequency comb output from a femtosecond fiber laser," *IEEE J. of Quantum Electron.* 41, 1388-1402 (2005).
- [31] Weiner, Andrew, *Ultrafast optics*. John Wiley & Sons, 2011.
- [32] A. Cingöz, D. C. Yost, T. K. Allison, A. Ruehl, M. E. Fermann, I. Hartl, and J. Ye, "Broadband phase noise suppression in a Yb-fiber frequency comb," *Opt. Lett.* 36, 743-745 (2011).
- [33] S. Namiki and H. A. Haus, "Noise of the Stretched Pulse Fiber Laser: Part I—Theory," *IEEE J. of Quantum Electronics* 33, 649-659 (1997).
- [34] C. X. Yu, S. Namiki and H. A. Haus, "Noise of the Stretched Pulse Fiber Laser: Part II—Experiments," *IEEE J. of Quantum Electronics* 33, 660-668 (1997).
- [35] Shu Namiki, Erich P. Ippen, Hermann A. Haus, and Charles X. Yu, "Energy rate equations for mode-locked lasers," *J. Opt. Soc. Am. B* 14, 2099-2111 (1997).
- [36] Jakob Fellingner, Aline S. Mayer, Georg Winkler, Wilfrid Grosinger, Gar-Wing Truong, Stefan Droste, Chen Li, Christoph M. Heyl, Ingmar Hartl, and Oliver H. Heckl, "Tunable dual-comb from an all-polarization-maintaining single-cavity dual-color Yb: fiber laser," *Opt. Express* 27, 28062-28074 (2019).

- [37] C. Jungwon Kim and Youjian Song, "Ultralow-noise mode-locked fiber lasers and frequency combs: principles, status, and applications," *Adv. Opt. Photon.* 8, 465-540 (2016).
- [38] Youjian Song, Chur Kim, Kwangyun Jung, Hyoji Kim, and Jungwon Kim, "Timing jitter optimization of mode-locked Yb-fiber lasers toward the attosecond regime," *Opt. Express* 19, 14518-14525 (2011).
- [39] G. C. Valley, "Photonic analog-to-digital converters," *Opt. Express* 15, 1955– 1982 (2007).
- [40] F. W. Wise, A. Chong, and W. H. Renninger, "High-energy femtosecond fiber lasers based on pulse propagation at normal dispersion," *Laser Photonics Rev.* 2(1-2), 58–73 (2008).
- [41] R. C. Jones, "A New Calculus for the Treatment of Optical Systems I. Description and Discussion of the Calculus," *J. Opt. Soc. Am.* 31(7), 488–493 (1941).
- [42] W. H. Knox, "Dispersion Measurements for Femtosecond-Pulse Generation and Applications," *Appl. Phys. B* 58, 225–235 (1994).
- [43] F. X. Kärtner, U. Morgner, T. Schibli, R. Ell, H. A. Haus, J. G. Fujimoto, and E. P. Ippen, "Few-cycle pulses directly from a laser," *Top. Appl. Phys.* 95, 73–136 (2004).
- [44] C. C. Harb, T. C. Ralph, E. H. Huntington, D. E. McClelland, H.-A. Bachor, and I. Freitag, "Intensity-noise dependence of Nd:YAG lasers on their diode-laser pump source," *J. Opt. Soc. Am. B* 14, 2936–2945 (1997).
- [45] C. C. Harb, T. C. Ralph, E. H. Huntington, I. Freitag, D. E. McClelland, and H. A. Bachor, "Intensity-noise properties of injection-locked lasers," *Phys. Rev. A* 54, 4370–4382 (1996).

- [46] D. von der Linde, "Characterization of the noise in continuously operating mode-locked lasers," *Appl. Phys. B* 39, 201–217 (1986).
- [47] Pandit, N., et al. "Characteristic instability of fibre loop soliton lasers," *Electronics Letters* 28, 455-457 (1992).
- [48] Wan, Chenchen, et al. "Intensity noise coupling in soliton fiber oscillators," *Optics letters* 42(24), 5266-5269 (2017).
- [49] Kang, Jin-U. and R. Sova. "Observation of dual relaxation-oscillations and their dynamics in all-PM erbium/ytterbium fibre ring-lasers," *Electronics Letters* 36, 1361-1362 (2000).
- [50] S. Salman, Y. Ma, K. Gürel, S. Schilt, C. Li, P. Pfäfflein, C. Mahnke, J. Fellingner, S. Droste, A. S. Mayer, O. H. Heckl, T. Südmeyer, C. M. Heyl, and I. Hartl, "Comparison of two low-noise CEP stabilization methods for an environmentally stable Yb: fiber oscillator," in *Laser Congress 2019 (ASSL, LAC, LS&C)* (The Optical Society of America, 2019), p. JTU3A.17.
- [51] L. Nugent-Glandorf, T. A. Johnson, Y. Kobayashi, and S. A. Diddams, "Impact of dispersion on amplitude and frequency noise in a Yb-fiber laser comb," *Opt. Lett.* 36, 1578–1580 (2011).
- [52] E. Portuondo-Campa, R. Paschotta, and S. Lecomte, "Sub-100 attosecond timing jitter from low-noise passively mode-locked solid-state laser at telecom wavelength," *Opt. Lett.* 38, 2650–2653 (2013).
- [53] D.A. Korobko, D.A. Stoliarov, P.A. Itrin, M.A. Odnoblyudov, A.B. Petrov, R.V. Gumenyuk, "Harmonic mode-locking fiber ring laser with a pulse repetition rate up to 12 GHz," *Optics & Laser Technology* 133, 0030-3992 (2021).

- [54] L. De la Cruz-May and E. Mejia-Beltran and A. Flores and J. A. Alvarez-Chavez and F. Martinez-Piñon, “Transparency power calculation in Yb<sup>3+</sup>-doped fiber due to temperature variations,” Proceedings of the 2nd Workshop on Specialty Optical Fibers and Their Applications (WSOF-2), 251-257 (2010).

# Appendix A

## Pump noise

Alex Murray measured the RIN of a laser diode of identical make and model as the one used to pump the laser discussed in this thesis. Fig. A.1 shows this laser diode's RIN, measured at different currents. The peak around 50 Hz was verified to result from a mechanical vibration in the measurement equipment, and not from the laser.

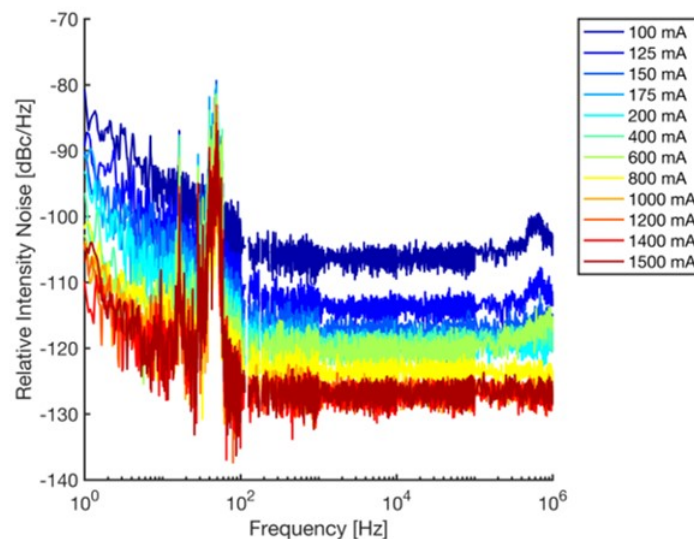


Figure A.1: RIN PSD of a laser diode identical to our laser's pump diode, measured at different currents (indicated in the legend). The peak around 50 Hz results from a mechanical vibration in the measurement equipment, and not from the laser.